



HAL
open science

Reticular Fibroblasts Expressing the Transcription Factor WT1 Define a Stromal Niche that Maintains and Replenishes Splenic Red Pulp Macrophages

Alicia Bellomo, Isabelle Mondor, Lionel Spinelli, Marine Lagueyrie, Benjamin J Stewart, Nicolas Brouilly, Bernard Malissen, Menna R Clatworthy, Marc Bajenoff

► **To cite this version:**

Alicia Bellomo, Isabelle Mondor, Lionel Spinelli, Marine Lagueyrie, Benjamin J Stewart, et al.. Reticular Fibroblasts Expressing the Transcription Factor WT1 Define a Stromal Niche that Maintains and Replenishes Splenic Red Pulp Macrophages. *Immunity*, 2020, 53 (1), pp.127 - 142.e7. 10.1016/j.immuni.2020.06.008 . hal-03013466

HAL Id: hal-03013466

<https://hal.science/hal-03013466>

Submitted on 23 Nov 2020

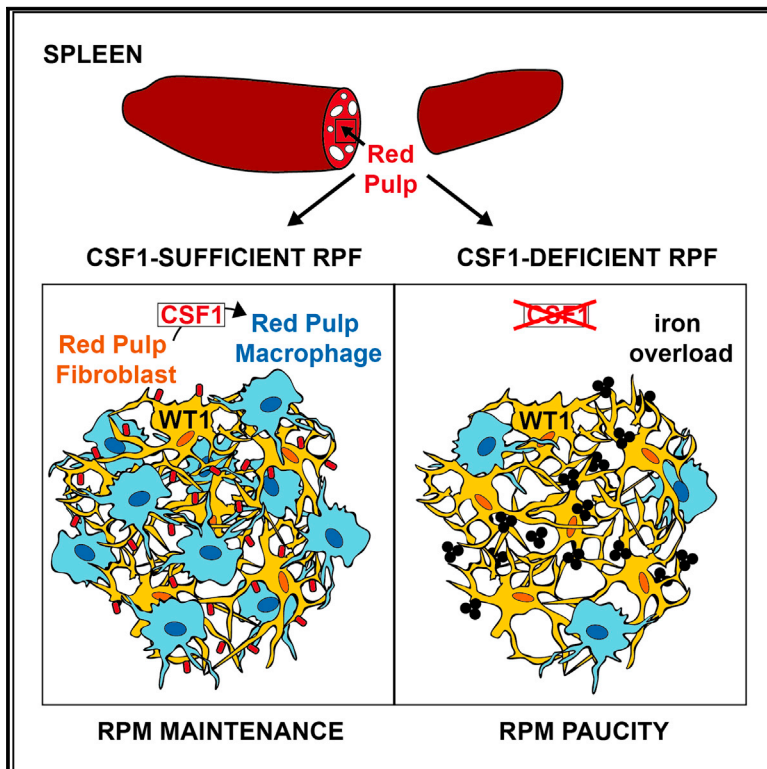
HAL is a multi-disciplinary open access archive for the deposit and dissemination of scientific research documents, whether they are published or not. The documents may come from teaching and research institutions in France or abroad, or from public or private research centers.

L'archive ouverte pluridisciplinaire **HAL**, est destinée au dépôt et à la diffusion de documents scientifiques de niveau recherche, publiés ou non, émanant des établissements d'enseignement et de recherche français ou étrangers, des laboratoires publics ou privés.

Immunity

Reticular Fibroblasts Expressing the Transcription Factor WT1 Define a Stromal Niche that Maintains and Replenishes Splenic Red Pulp Macrophages

Graphical Abstract



Authors

Alicia Bellomo, Isabelle Mondor, Lionel Spinelli, ..., Bernard Malissen, Menna R. Clatworthy, Marc Bajénoff

Correspondence

bajenoff@ciml.univ-mrs.fr

In Brief

Bellomo et al. demonstrate that homeostasis of splenic red pulp macrophages and iron metabolism are regulated by a reticular meshwork of red pulp fibroblasts characterized by the expression of Wilms' Tumor 1 and colony stimulating factor 1.

Highlights

- RPMs are embedded in a meshwork of WT1, CSF1-expressing RP fibroblasts
- RP fibroblasts represent a unique subset of splenic stromal cells
- RP-fibroblast-derived CSF1 controls homeostasis of RPMs
- RP fibroblasts participate to the recruitment of monocytes



Article

Reticular Fibroblasts Expressing the Transcription Factor WT1 Define a Stromal Niche that Maintains and Replenishes Splenic Red Pulp Macrophages

Alicia Bellomo,¹ Isabelle Mondor,¹ Lionel Spinelli,¹ Marine Lagueyrie,¹ Benjamin J. Stewart,^{2,3,4} Nicolas Brouilly,⁵ Bernard Malissen,¹ Menna R. Clatworthy,^{2,3,4} and Marc Bajénoff^{1,6,*}

¹Aix Marseille Univ, CNRS, INSERM, CIML, Marseille, France

²Molecular Immunity Unit, Department of Medicine, University of Cambridge, Cambridge, UK

³Cambridge University Hospitals NHS Foundation Trust and NIHR Cambridge Biomedical Research Centre, Cambridge, UK

⁴Wellcome Sanger Institute, Wellcome Genome Campus, Hinxton, UK

⁵Aix-Marseille Université, Centre National de la Recherche Scientifique, Institut de Biologie du Développement de Marseille, Marseille, France

⁶Lead Contact

*Correspondence: bajenoff@ciml.univ-mrs.fr

<https://doi.org/10.1016/j.immuni.2020.06.008>

SUMMARY

Located within red pulp cords, splenic red pulp macrophages (RPMs) are constantly exposed to the blood flow, clearing senescent red blood cells (RBCs) and recycling iron from hemoglobin. Here, we studied the mechanisms underlying RPM homeostasis, focusing on the involvement of stromal cells as these cells perform anchoring and nurturing macrophage niche functions in lymph nodes and liver. Microscopy revealed that RPMs are embedded in a reticular meshwork of red pulp fibroblasts characterized by the expression of the transcription factor Wilms' Tumor 1 (WT1) and colony stimulating factor 1 (CSF1). Conditional deletion of *Csf1* in WT1⁺ red pulp fibroblasts, but not white pulp fibroblasts, drastically altered the RPM network without altering circulating CSF1 levels. Upon RPM depletion, red pulp fibroblasts transiently produced the monocyte chemoattractants CCL2 and CCL7, thereby contributing to the replenishment of the RPM network. Thus, red pulp fibroblasts anchor and nurture RPM, a function likely conserved in humans.

INTRODUCTION

All organs contain macrophages that sustain tissue homeostasis within the body, not only as immune cells but also through trophic, regulatory, and repair functions (Varol et al., 2015). The spleen is a compartmentalized lymphoid tissue composed of the white pulp (WP) that is surrounded by a venous part, the red pulp (RP) (Golub et al., 2018; Mebius and Kraal, 2005). Splenic arterioles and capillaries do not connect to venules in the RP but discharge their content into unique structures known as the RP cords. These labyrinthine structures form an intermediate circulation between the capillaries and venous sinuses and are populated by RP macrophages (RPMs) (Kurotaki et al., 2015). Although RPMs are involved in host defense, they are primarily known to scavenge senescent erythrocytes and recycle their hemoglobin iron, thus participating in iron metabolism (Kurotaki et al., 2015). Recent studies have revealed that RPMs are generated during embryogenesis and are maintained throughout adult life with negligible input from monocytes (Epelman et al., 2014; Hashimoto et al., 2013). However, we still lack a comprehensive understanding of the mechanisms supporting their homeostasis.

Macrophages depend on environmental cues such as the chemokine CX3CL1, interleukin (IL) 34, colony stimulating factor

(CSF)1, and CSF2 for their development and maintenance (Lavin et al., 2015). These molecules are thought to be produced by “macrophage niches” within tissues, which provide a three-dimensional anchoring scaffold for macrophages and nurture them by cytokine production (Guilliams and Scott, 2017; Guilliams et al., 2020; T'Jonck et al., 2018). In return, macrophages should provide positive “feedback” signals to their niche, generating two-cell circuits that mutually benefit each partner (Zhou et al., 2018). Although this concept has recently found wide acceptance in the field, the nature of these niches remains elusive in most tissues, including the spleen.

Lymphoid stromal cells comprise essential components of the macrophage niche in lymph nodes. By using a combination of imaging techniques and conditional mouse models, we and others have shown that lymphatic endothelial cells (LECs) regulate the homeostasis of lymph-node subcapsular and medullary macrophages via the production of CSF1 (Mondor et al., 2019) and receptor activator of nuclear factor κ B (RANK) (Camara et al., 2019; Mondor et al., 2019). Because LECs are absent from the spleen, we hypothesized that a different type of stromal cells might regulate RPM homeostasis in this organ.

The stromal compartment of the splenic WP is supported by mesenchymal stromal cells collectively known as fibroblastic



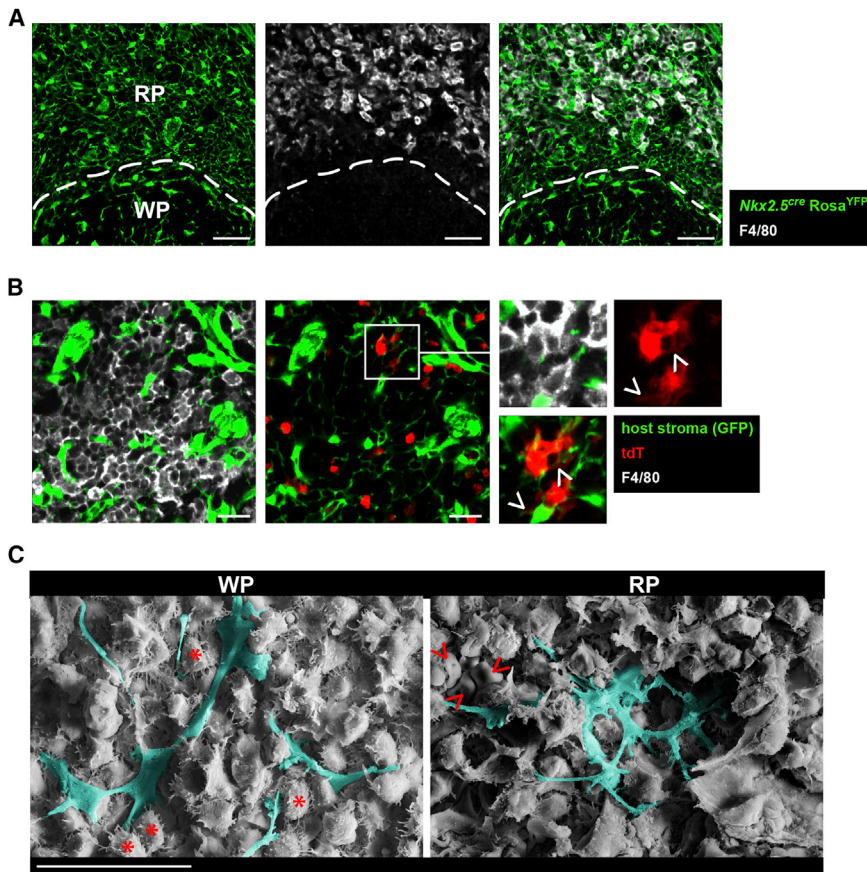


Figure 1. Mesenchymal Reticular Cells Form a Dense Network in the Splenic Red Pulp

(A) Spleen sections isolated from *Nkx2.5^{Cre} Rosa^{YFP}* mice were stained for F4/80 expression and analyzed by confocal microscopy. Scale bar, 40 μ m. Dashed line represents the WP/RP boundary. Data are representative of 2 experiments; n = 4.

(B) Adult *Ubc^{GFP}* mice were sub-lethally irradiated and reconstituted with a mixture of BM cells isolated from wild-type (99%) and *Cx3cr1^{Cre} Rosa^{tdT}* (1%) mice, allowing the identification of single tdT⁺ RPMs and their cellular processes in relation to the host GFP⁺ stromal network. One month later, spleens were stained for F4/80 expression. Scale bar, 20 μ m. Arrowheads point to tdT⁺ RPM cellular processes stretching over GFP⁺ reticular cells. Data are representative of 2 experiments; n = 5 mice.

(C) Representative pictures of fibroblastic cells (blue) imaged by scanning electron microscopy in the white (left) and red (right) pulp of an adult mouse spleen. Asterisks and arrowheads point to lymphocytes and RBC, respectively. Scale bar, 20 μ m. Data are representative of 2 experiments; n = 4 mice.

reticular cells (FRCs). T and B cell zones are populated by several types of T-cell-zone reticular fibroblasts (TRCs) and follicular dendritic cells (FDCs) controlling the migration and homeostasis of T and B cells (Mueller and Germain, 2009). Marginal reticular cells (MRCs) are the stromal cells of the marginal zone that overlie B cell follicles and are thought to represent the adult counterparts of embryonic lymphoid-tissue organizer cells (Jarjour et al., 2014; Katakai et al., 2008). Although it is appreciated that the RP is composed of a three-dimensional network of splenic cords and venous sinuses, its stromal cell compartment is much less characterized (Mebius and Kraal, 2005). Venous sinuses are found throughout the RP and are lined by loose endothelial cells. The splenic cords are formed by reticular fibers and reticular cells that have been observed in many species, but little is known about their function because of the absence of adequate tools (Chen and Weiss, 1972; Cheng et al., 2019; Suzuki, 1972; Suzuki et al., 1977). As RPMs reside within these splenic cords, these enigmatic RP reticular cells could represent their niche.

Here, we sought to identify the cellular niche of RPMs. We characterized the most abundant population of RP mesenchymal stromal cells in the spleen as fibroblasts specifically expressing the transcription factor Wilms' Tumor 1 (WT1). RP fibroblasts formed an extensive cellular meshwork in which RPMs are embedded. Conditional deletion of CSF1 in RP fibroblasts, but not WP fibroblasts, impaired RPMs and iron homeostasis without altering circulating levels of CSF1. RP fibroblasts were the main source of CSF1 in the murine and human spleen and

were central to the replenishment of the RPM network after depletion via abundant but transient production of monocyte chemoattractants and subsequent recruitment of blood monocytes. Altogether, our results identified splenic RP fibroblasts as an essential component of the RPM niche.

RESULTS

RPMs Are Embedded in a Dense Network of Mesenchymal Stromal Cells

RPMs reside in the open blood circulation of the spleen and are thus exposed to constant shear stress (Kohyama et al., 2009; Kurotaki et al., 2015). This unique location suggests the existence of an anchoring mesenchymal network to which RPMs are attached. We sought to further characterize this network by using *Nkx2.5^{Cre} Rosa^{YFP}* mice. In these mice, embryonic mesenchymal cells with lymphoid-tissue organizer activity acquire yellow fluorescent protein (YFP) expression after Cre-mediated recombination. Because all mesenchymal splenic stromal cells derive from these progenitors, they are lineage traced as YFP⁺ cells in these mice (Castagnaro et al., 2013). Confocal imaging of *Nkx2.5^{Cre} Rosa^{YFP}* spleens revealed that RPMs were indeed embedded in a dense meshwork of YFP⁺ mesenchymal cells (Figure 1A). We then generated bone marrow (BM) chimeras in which the radioresistant host stroma and donor BM-derived RPMs were labeled in distinct fluorescent colors. This approach revealed that the extracellular processes of tdTomato (tdT)⁺ RPMs were juxtaposed to the ones of GFP⁺ RP reticular cells, suggesting a close interaction between the two partners (Figure 1B). Finally, we used scanning electron

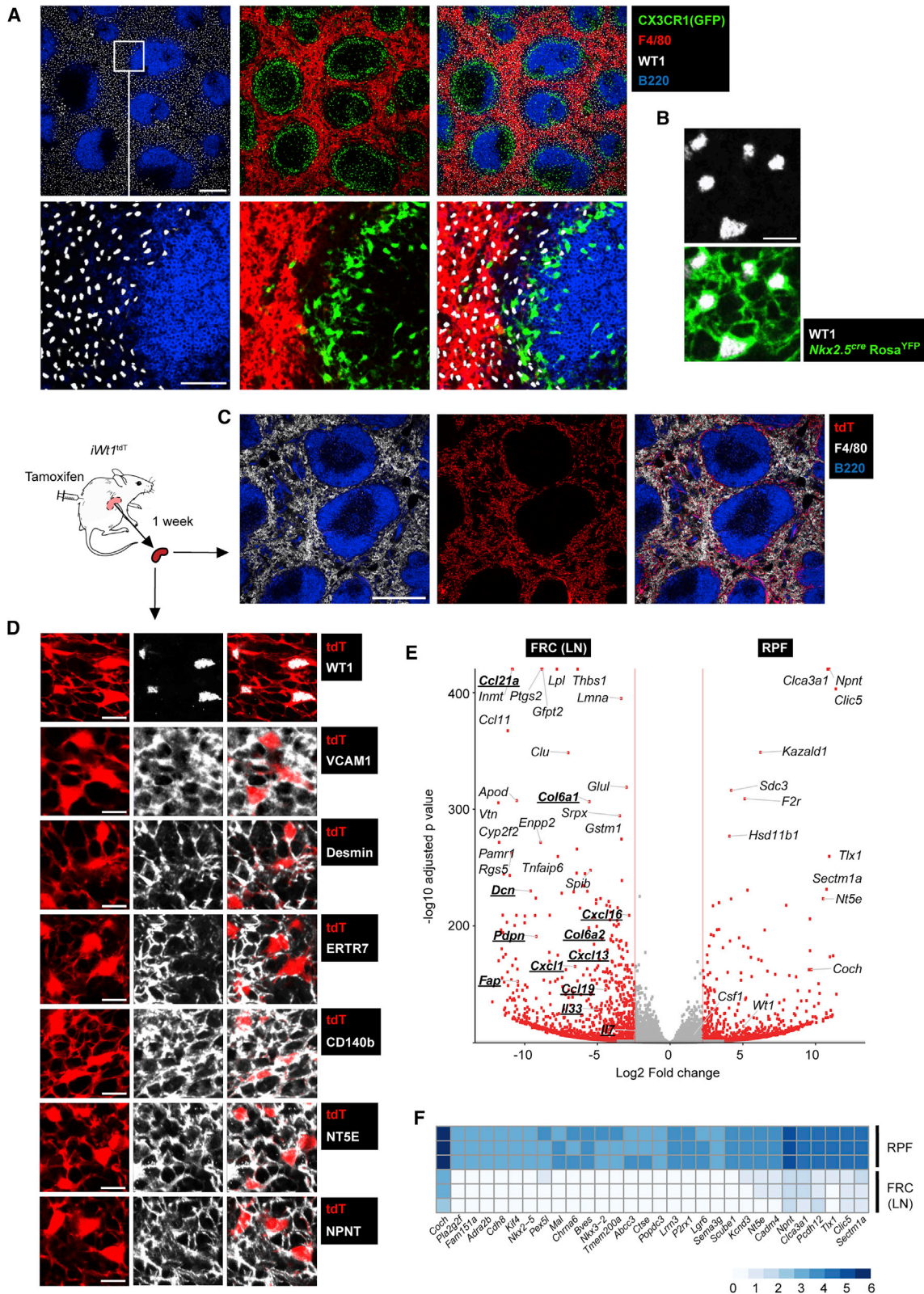


Figure 2. Characterization of WT1-Expressing RP Fibroblasts

(A) Spleen sections of *Cx3cr1*^{GFP/+} mice were stained for F4/80, B220, and WT1 expression. Scale bars, 200 μ m (upper panels), 50 μ m (lower panels). Data are representative of 2 experiments; n = 6.

microscopy to compare the morphology of WP and RP reticular cells. Although the density of the reticular network was higher in the RP (Figure 1A), both cell types displayed similar elongated spindle shapes characteristic of fibroblastic networks in lymphoid organs (Figure 1C).

RP Mesenchymal Cells Are Wilms'-Tumor-1-Expressing Fibroblasts

The network of RP reticular cells has previously been observed and partially characterized in several species (Chen and Weiss, 1972; Cheng et al., 2019; Suzuki, 1972; Suzuki et al., 1977). However, in absence of proper tools and markers allowing their isolation, the biological functions of RP reticular cells remained elusive. We thus sought to identify markers and mouse models allowing their manipulation *in vivo*. WT1 is a transcription factor that regulates spleen development (Kim et al., 1999). *Wt1*-deficient mice are asplenic, and conditional deletion of *Wt1* in adult mice leads to severe splenic atrophy (Chau et al., 2011). Adult mouse spleens were thus immunostained for WT1 expression. We found that WT1 was abundantly present in the RP and virtually absent from the WP (Figure 2A). Additional stainings performed in *Nkx2.5^{Cre} Rosa^{YFP}* mice showed that WT1 was expressed in the nucleus of YFP⁺ RP reticular cells, thus identifying WT1 as a useful marker for this stromal cell subset (Figure 2B). We further took advantage of *Wt1^{CreERT2} Rosa^{tdT} (iWt1^{tdT})* mice to characterize RP reticular cells by imaging and flow cytometry (Zhou et al., 2008). Injection of tamoxifen in *iWt1^{tdT}* mice triggered tdT expression in the RP only (Figure 2C). Within the RP, tdT⁺-labeled cells formed a reticular meshwork expressing WT1, VCAM1 (CD106), desmin, ERTR7, and PDGFR (CD140) α and β but not podoplanin (gp38) and CD31 (Figures 2D and S1A). Based on these results, we designed an antibody panel allowing the identification of RP reticular cells by flow cytometry. As indicated in Figures 2D and S1A, splenic RP reticular cells could be defined as CD45⁻ CD31⁻ gp38⁻ VCAM1⁺ WT1⁺ cells.

Transcriptomic Analysis Confirms Fibroblastic Identity of RP Reticular Cells

We first sought to characterize RP reticular cells in detail by comparing them to FRCs, a stereotypical subset of lymphoid fibroblasts. We chose to use lymph node (LN) FRCs based on findings made in *Ccl19^{Cre} Rosa^{YFP}* mice. In this model, splenic WP and LN FRCs homogeneously express YFP by imaging (Chai et al., 2013; Cheng et al., 2019). However, by flow cytometry, only a fraction of splenic FRCs expressed YFP, whereas virtually all LN FRCs were labeled, in keeping with imaging results (Chai et al., 2013; Cheng et al., 2019). Because of this

discrepancy, we used LN as a source of FRC. We thus compared the gene expression profiles of tdT⁺ RP reticular cells to that of CD45⁻ CD31⁻ gp38⁺ tdT⁻ LN FRCs isolated from tamoxifen-treated *iWt1^{tdT}* mice (Figure S1A). Bulk RNA-sequencing analysis indicated that RP reticular cells and FRCs shared many genes encoding fibroblast-specific molecules such as collagens, laminins, and adhesion molecules (Figure S1B), confirming the fibroblastic nature of RP reticular cells. However, FRCs and RP fibroblasts also showed divergent expression of many genes, including immune genes (Figures 2E and 2F). RP fibroblasts expressed lower levels of *Ccl21a*, *Ccl19*, *Cxcl16*, *Cxcl13*, and *Ilf7*, genes involved in leukocyte migration and survival (Coelho et al., 2013; Hara et al., 2006; Link et al., 2007; Okada and Cyster, 2007). RP fibroblasts also expressed lower levels of *Pdpr* (podoplanin, gp38) and *Fap* genes controlling contraction and growth of myofibroblasts as well as anchoring of dendritic cells (DCs) on the FRC network (Acton et al., 2014; Astarita et al., 2015). These results suggested that RP fibroblasts were not endowed with T, B, or DC regulatory functions normally associated with TRCs or FDCs. In order to compare the transcriptome of RP fibroblasts to that of other splenic stromal cells, we took advantage of single-cell RNA-sequencing (scRNA-seq) datasets generated by Ludwig and colleagues (Cheng et al., 2019). We first confirmed expression of WT1 by RP fibroblasts and found that they were closely related to splenic mural cells, a population of perivascular cells surrounding splenic blood vessels (Figure S1C, upper panels) (Cheng et al., 2019). Although our WT1⁺-expressing RP fibroblasts clustered with a single population of fibroblasts identified by scRNA-seq analysis, we investigated whether they nonetheless harbored any heterogeneity. Despite the fact that RP fibroblasts could be further subdivided into 5 clusters, the genes distinguishing these clusters corresponded to a signature induced by mild dissociation stress, known to be a technical noise factor in scRNA-seq data (van den Brink et al., 2017) (not shown). In addition, there was uniform expression of the markers used to sort these cells across all identified clusters, with homogeneous expression of *Wt1* and *Csf1*, suggesting that RP fibroblasts constituted a homogeneous population of stromal cells (Figure S1C, lower panels). Next, we aimed to leverage our transcriptomic data for insights into the functions of RP fibroblasts. We did so by analyzing the transcription factor regulons defining the different stromal cell types by using the Pyscenic framework (Aibar et al., 2017) and identified strong enrichment for a *Wt1*-governed regulon specifically in RP fibroblasts (Figure S1D), in keeping with our biological data. This RP-fibroblast-specific *Wt1* regulon characterizing RP fibroblasts was enriched for genes related to mesenchymal differentiation and endothelial cell function (Figure S1D), consistent with their location at the

(B) Spleen sections isolated from *Nkx2-5^{Cre} Rosa^{YFP}* mice were stained for WT1 expression. Scale bar, 10 μ m. Data are representative of 2 experiments; n = 4. (C and D) Adult *iWt1^{tdT}* mice were treated with tamoxifen. One week later, spleen sections were stained for F4/80 and B220 expression (C) or for the indicated markers (D). Scale bars, 400 μ m (C), 10 μ m (D). Data are representative of 2 experiments; n = 6.

(E and F) Transcriptomic analysis. Lymph node FRCs and RP fibroblasts were isolated by flow cytometry and analyzed by bulk RNA-seq.

(E) Volcano plot depicting the top differentially expressed genes between FRCs and RP fibroblasts. The x axis shows the fold change (log₂) of normalized mean gene expression across replicates of RP fibroblasts versus FRCs (right: RP fibroblast overexpression, left: FRC). The y axis shows the $-\log_{10}$ of the adjusted p value of the differential expression test (see STAR Methods). Genes belonging to the core signature of FRCs are bolded and underlined. See also Figures S1 and S2.

(F) Heatmap of normalized mean gene expression across replicates for the 30 genes expressed the highest by RP fibroblasts with respect to FRCs (see STAR Methods).

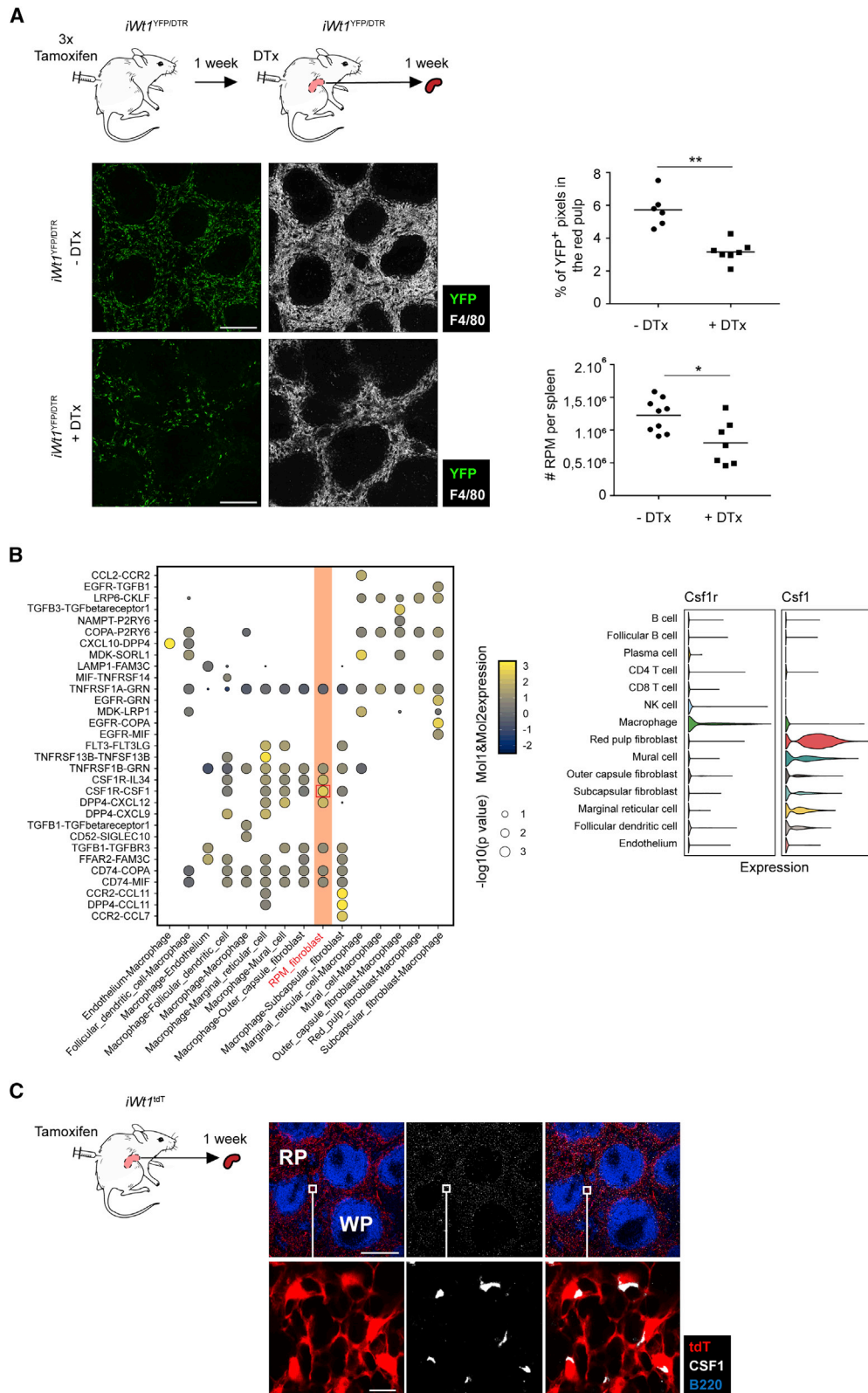


Figure 3. RP Fibroblasts Regulate RPM Density

(A) Adult $iWt1^{YFP/DTR}$ mice were treated with tamoxifen and injected one week later with diptheria toxin (+DTx) or not (-DTx). Another week later, their spleens were stained for F4/80 and YFP expression and analyzed by flow cytometry and confocal imaging. Depletion of YFP⁺ RP fibroblasts and loss of F4/80⁺ RPMs

(legend continued on next page)

interface with the circulation. Finally, we interrogated the existence of RP fibroblasts in human spleen by scRNA-seq analysis of CD45⁻-enriched human splenocytes. As indicated in [Figure S2](#), RP fibroblasts were readily identified, demonstrating that WT1⁺ RP fibroblasts also exist in humans.

Deletion of RP Fibroblasts Compromises the RPM Network

We hypothesized that RP fibroblasts could represent an anchoring and nurturing scaffold for RPMs. In this scenario, ablating RP fibroblasts should alter RPM homeostasis and cause a decrease in their numbers. To test this hypothesis, we designed a mouse model allowing conditional deletion of RP fibroblasts *in vivo*. In *Wt1*^{CreERT2} Rosa^{DTR} Rosa^{YFP} (*Wt1*^{YFP/DTR}) mice, tamoxifen induces co-expression of YFP and diphtheria toxin receptor (DTR) in WT1-expressing cells. Adult mice treated with tamoxifen were injected or not with Diphtheria toxin (DTx) one week later. The efficacy of RP fibroblast deletion as well as its consequence on RPMs (defined as CD45⁺ CD11b^{lo} F4/80⁺ CD64^{hi} VCAM1^{hi} MHCII^{lo} cells) were analyzed by confocal imaging and flow cytometry another week later, the time point we identified as the peak of RP fibroblast deletion. Injection of DTx deleted 45% of YFP⁺ RP fibroblasts and induced a concomitant proportional loss of RPMs (41%) ([Figures 3A and S3A](#)). Critically, we confirmed that RPMs did not express YFP and were not affected in DTx-treated control mice ([Figures S3B and S3C](#)). We thus concluded that alteration of the RP fibroblastic network compromises RPM homeostasis.

RP Fibroblasts Regulate RPM Homeostasis via CSF1

As we postulated that RP fibroblasts contribute to the niche of RPMs, their partial deletion in *Wt1*^{YFP/DTR} mice might have impacted the RPM network in different ways: RPMs might have lost their anchoring scaffold, their source of survival signals, or both. Macrophage niches are thought to control macrophage adhesion and survival through a variety of soluble and membrane-bound molecules, such as CX3CL1, IL34, CSF1, and CSF2 ([Lavin et al., 2015](#)). In order to identify the molecular mechanisms underlying the dialog established between RP fibroblasts and RPMs, we analyzed their transcriptome with the CellPhoneDB tool, a dedicated resource for inferring cell-cell communication from combined expression of multi-subunit receptor-ligand complexes ([Egen et al., 2008](#); [Vento-Tormo et al., 2018](#)). Among other factors, we found that *Csf1* and its receptor *Csf1r* were expressed at particularly high levels by RP fibroblasts and RPMs, respectively ([Figure 3B](#)). CSF1 is the major survival factor of macrophages *in vivo*. Although CSF1-deficient (*Csf1*^{op/op}) mice display a drastic paucity of resident macrophages across organs, CSF2-, CX3CL1-, and IL34-deficient mice only suffer from discrete macrophage alterations ([Cecchini et al., 1994](#); [Chitu and Stanley, 2006](#); [Dai](#)

[et al., 2002](#); [Greter et al., 2012](#); [Medina-Contreras et al., 2011](#); [Schneider et al., 2014](#)). We thus assessed local production of CSF1 in the spleen of tamoxifen-treated *Wt1*^{tdT} mice by confocal imaging ([Figure 3C](#)). CSF1 immunostaining could be detected almost exclusively in the RP, where it largely overlapped with RP fibroblasts. Indeed, quantification revealed that ~75% of tdT⁺ RP fibroblasts expressed CSF1 in their cytoplasm (292 out of 392 cells). We therefore interrogated the physiological role of RP-fibroblast-derived CSF1 in RPM homeostasis by using genetic tools. This was achieved by generating *Wt1*^{Cre} mice bearing conditional “floxed” alleles of *Csf1* ([Harris et al., 2012](#); [Zhou et al., 2008](#)). *Cc19*^{ΔCsf1} mice, in which Cre is expressed by WP fibroblasts, served as controls ([Figure S4A](#)) ([Chai et al., 2013](#)). As expected, CSF1 was produced at normal levels in the RP of *Cc19*^{ΔCsf1} mice ([Figure 4A](#)), and RPMs were not affected ([Figures 4A and 4B](#)). On the contrary, CSF1 expression was strongly reduced (~20% of the control) in the RP of *Wt1*^{ΔCsf1} mice, and *Csf1* mRNA was no longer detectable in splenic RP fibroblasts isolated from *Wt1*^{ΔCsf1} mice ([Figure S4B](#)). In line with our hypothesis, conditional deletion of *Csf1* in RP fibroblasts was accompanied by a 75% reduction of RPM density ([Figures 4A and 4B](#)). RPMs are known to degrade senescent erythrocytes and recycle heme-associated iron, making them important regulators of iron metabolism ([Haldar et al., 2014](#); [Kohyama et al., 2009](#)). Accordingly, we found that *Wt1*^{ΔCsf1} mice developed iron overload localized to the splenic RP ([Figure 4C](#)).

It remained conceivable that deletion of *Csf1* in WT1-Cre-expressing cells impacted circulating levels of CSF1 and thereby indirectly altered RPM homeostasis. We addressed this possibility by measuring circulating levels of CSF1 and the number of blood monocytes in *Wt1*^{ΔCsf1} mice. Levels of circulating CSF1 and monocyte counts were normal in these mice, ruling out a major role of systemic CSF1 levels in the regulation of RPM homeostasis ([Figures 4D and 4E](#)). Despite being a long-established tool for genetic manipulation, the Cre-lox recombination system displays some caveats linked to Cre toxicity in certain cell types, including immune cells such as mast cells ([Feyerabend et al., 2011](#)). As WT1 is expressed in a subset of hematopoietic progenitors ([Chau et al., 2011](#)), RPMs themselves might have been killed by Cre action in *Wt1*^{ΔCsf1} mice. Alternatively, some macrophages have been reported to express CSF1, raising the possibility that RPMs were no longer able to sustain their own survival in these mice ([DeFalco et al., 2015](#)). These hypotheses were tested in mixed competitive BM chimeras. Wild-type mice were fully irradiated and reconstituted with a mixture (~50/50) of BM cells isolated from control and *Wt1*^{ΔCsf1} mice bearing different fluorescent reporters. Two months later, chimeric spleens were analyzed by flow cytometry. We found that like neutrophils, T cells, and monocytes, RPMs were generated in the same proportions by both genotypes, ruling out these two RPM-intrinsic effects ([Figure 4F](#)).

were determined by imaging and flow cytometry, respectively. Scale bars, 300 μm. Dots represent individual mice. Pooled data are from 2 independent experiments; n = 9 (-DTx) and n = 7 (+DTx). Bars = means. See also [Figure S3](#).

(B) Left panel: heatmap of predicted chemokine ligand-receptor interactions between stromal and macrophage populations identified in murine spleen scRNA-seq datasets. Point size indicates CellPhoneDB permutation p value, point color indicates the scaled aggregate expression value of genes in each ligand-receptor complex. Right panel: Violin plots showing expression levels of *Csf1r* and *Csf1* in populations of cells identified in murine spleen scRNA-seq datasets ([Cheng et al., 2019](#)).

(C) Adult *Wt1*^{tdT} mice were treated with tamoxifen. One week later, spleen sections were stained for CSF1 expression. Insets show intracellular CSF1 staining of tdT⁺ RP fibroblasts. Scale bars, 400 μm (upper panels), 10 μm (lower panels). Data are representative of 2 experiments; n = 6.

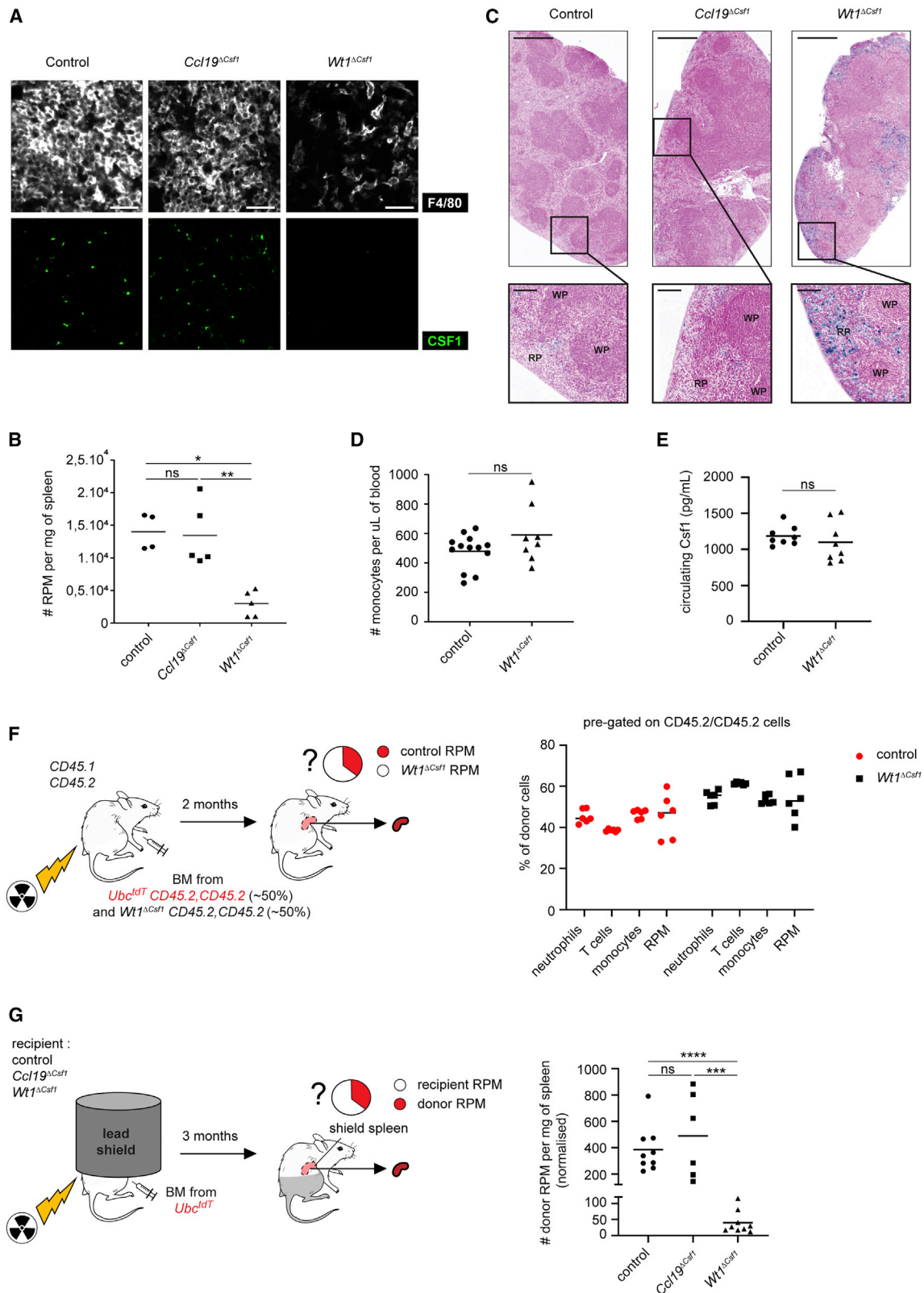


Figure 4. RP-Fibroblast-Derived CSF1 Regulates RPM Homeostasis

(A) Wild-type spleens and spleens of *Wt1^{cre}* and *Ccl19^{cre}* mice bearing conditional alleles of *Csf1* (*Wt1^{ΔCsf1}* and *Ccl19^{ΔCsf1}*) were stained for F4/80 and CSF1 expression. Scale bars, 30 μ m. Data are representative of 3 experiments; $n \geq 12$. See Figure S4A.

The alteration of the RPM network observed in adult $Wt1^{\Delta Csf1}$ mice could be the consequence of a developmental defect in addition to an incapability of RP fibroblasts to sustain homeostasis of adult RPMs. In keeping with a developmental defect, RPMs were drastically reduced (50%–75%) in the spleens of $Wt1^{\Delta Csf1}$ neonates (P0 and P7) (Figure S4C). In order to specifically assess the homeostatic role of RP-fibroblast-derived CSF1 on RPM homeostasis and delineate it from this developmental defect, we generated shielded BM chimeras, in which splenic stromal cells were not affected by irradiation and thus remained of host origin (Baratin et al., 2017). The spleens of adult wild-type, $Ccl19^{\Delta Csf1}$, and $Wt1^{\Delta Csf1}$ mice were protected by a lead tube, and mice were irradiated and reconstituted with fluorescent wild-type BM cells, allowing engraftment and identification of donor-derived RPMs in the protected spleens (Figure 4G). Three months later, we found that BM-derived RPMs were drastically reduced (90%) only in $Wt1^{\Delta Csf1}$ recipient mice, demonstrating that adult spleens containing *Csf1*-deficient RP fibroblasts were no longer able to sustain RPM homeostasis. Of note, a similar decrease (50%) of RPMs was recently observed in the spleen of adult mice treated for one week with an antibody blocking CSF1, independently confirming the role of CSF1 in the maintenance of these macrophages (Lin et al., 2019). Although $Wt1^{\Delta Csf1}$ mice displayed normal levels of circulating monocytes, myelopoiesis might be partially compromised in the BM of these mice. We therefore first investigated the presence of WT1⁺ fibroblasts in the bones of $iWT1^{tdT} Cx3cr1^{GFP/+}$ adult mice treated 10 days before with tamoxifen. As indicated in Figure S4D, tdT⁺ fibroblasts were absent from the bones of these mice but abundantly present in their spleen. Accordingly, we found that numbers of BM monocyte progenitors and macrophages were comparable between $Wt1^{\Delta Csf1}$ and control mice (Figures S4E and S4F). By using various mouse models and *in vitro* studies, Buechler and colleagues identified retinol-producing WT1-expressing stromal cells as a niche imprinting large cavity-resident macrophages (Buechler et al., 2019). We reasoned that cavity-resident WT1⁺ cells might not only imprint peritoneal macrophages but also control their homeostasis via the provision of CSF1. In line with this, we found that pleural and peritoneal large cavity macrophages were drastically reduced in $Wt1^{\Delta Csf1}$ mice (97% and 66% of reduction respectively; Figure S4G), suggesting that WT1 might represent a factor globally specifying the transcriptional landscape of several macrophage niches.

In order to rule out the contribution of an additional source of CSF1 to RPM homeostasis, we compared the levels of tran-

scripts encoding soluble and membrane bound *Csf1* in splenic RP fibroblasts to that of splenic FRC, vascular endothelial cells (VECs) and CD45⁺ hematopoietic cells isolated from control, $Wt1^{\Delta Csf1}$, and $Ccl19^{\Delta Csf1}$ mice (Figure S4B). As expected, both CSF1 isoforms were abundantly expressed in control RP fibroblasts but not detected in control CD45⁺ hematopoietic cells, confirming the stromal origin of CSF1. We further determined that VECs expressed small amounts of membrane-bound *Csf1* and took advantage of $Cdh5^{\Delta Csf1}$ mice to assess the contribution of endothelial-derived CSF1 to RPM homeostasis. Although homeostasis of LN subcapsular sinus macrophages was perturbed in these mice upon tamoxifen treatment (Figure S4H), in keeping with our previous work (Mondor et al., 2019), numbers of RPMs were unaffected, ruling out a contribution of endothelial-derived CSF1 to the homeostasis of RPMs (Figure S4I). Collectively, these results corroborated that RP fibroblasts control RPM homeostasis through local production of CSF1, making them essential components of the splenic RPM niche.

Marginal Zone Macrophages and Metallophilic Macrophages Depend on CSF1

The spleen is populated by three additional subsets of macrophages. The marginal zone (MZ) harbors Marco⁺ Marginal zone macrophages (MZMs) in the outer MZ and CD169⁺ Metallophilic macrophages (MMMs) in the inner MZ, whereas MertK⁺ T zone macrophages (TZMs) locate to the T cell zone (A-Gonzalez and Castrillo, 2018). We analyzed the distribution of these macrophages in the spleens of control, $Wt1^{\Delta Csf1}$, and $Ccl19^{\Delta Csf1}$ mice (Figure S5A). Confocal imaging revealed that MZMs and TZMs were present in normal numbers in the spleen of $Ccl19^{\Delta Csf1}$ mice, whereas MMMs were absent, suggesting that CSF1 produced by splenic RP fibroblasts (Figure S4B) contributed to MMM homeostasis. Although we determined that MRCs co-localized with MMMs and produced CSF1 (Figure 3B), the exact niche of MMMs remains to be identified with refined tools. Interestingly, both MMMs and MZMs were affected in $Wt1^{\Delta Csf1}$ mice, suggesting that RP fibroblasts or another WT1-expressing stromal cell type located in the MZ represented the niche of MZMs (Figures 2A and S5A).

RP Fibroblasts Contribute to the Replenishment of the RPM Network

Macrophage networks can be transiently altered by insults such as infections (Blériot et al., 2015; Lai et al., 2018; Robinson et al., 2012). In many organs including liver, lymph nodes, skin, and

(B) RPM numbers in the spleens of control, $Ccl19^{\Delta Csf1}$ and $Wt1^{\Delta Csf1}$ adult mice were determined by flow cytometry. Dots represent individual mice. Data are representative of 3 experiments; $n \geq 12$. Bars = means.

(C) Adult wild-type, $Wt1^{\Delta Csf1}$, and $Ccl19^{\Delta Csf1}$ spleens were stained for ferric iron (blue). Iron overload was only observed in the RP of $Wt1^{\Delta Csf1}$ mice. Scale bar, 500 μm (top), 100 μm (bottom). Data are representative of 3 experiments; $n \geq 5$.

(D) Numbers of blood monocytes (defined as CD45⁺ Ly6G⁻ SSC-A^{lo} CD115⁺ CD11b^{hi} cells) were determined by flow cytometry. Dots represent individual mice. Pooled data are from 2 independent experiments; $n = 13$ (control) and $n = 7$ ($Wt1^{\Delta Csf1}$). Bars = means.

(E) Circulating levels of CSF1 were quantified by ELISA. Dots represent individual mice. Bars = means. Pooled data are from 2 independent experiments; $n = 8$ (control) and $n = 8$ ($Wt1^{\Delta Csf1}$). See Figure S4B.

(F) Adult CD45.1/CD45.2 mice were sub-lethally irradiated and reconstituted with a mixture of BM cells isolated from CD45.2/CD45.2 Ubc^{tdT} (~50%) and CD45.2/CD45.2 $Wt1^{\Delta Csf1}$ (~50%) mice. The level of chimerism in the indicated donor cell types was determined 2 months later by flow cytometry. Dots represent individual mice. Data are representative of 2 experiments; $n = 6$. Bars = means.

(G) $Wt1^{\Delta Csf1}$, $Ccl19^{\Delta Csf1}$, and control adult mice were shield irradiated and reconstituted with Ubc^{tdT} BM cells. Three months later, the number of tdT⁺ donor RPMs per mg of spleen in shielded spleens was assessed by flow cytometry. Dots represent individual mice. Pooled data are from 2 independent experiments; $n = 9$ (control), $n = 6$ ($Ccl19^{\Delta Csf1}$), and $n = 9$ ($Wt1^{\Delta Csf1}$). Bars = means.

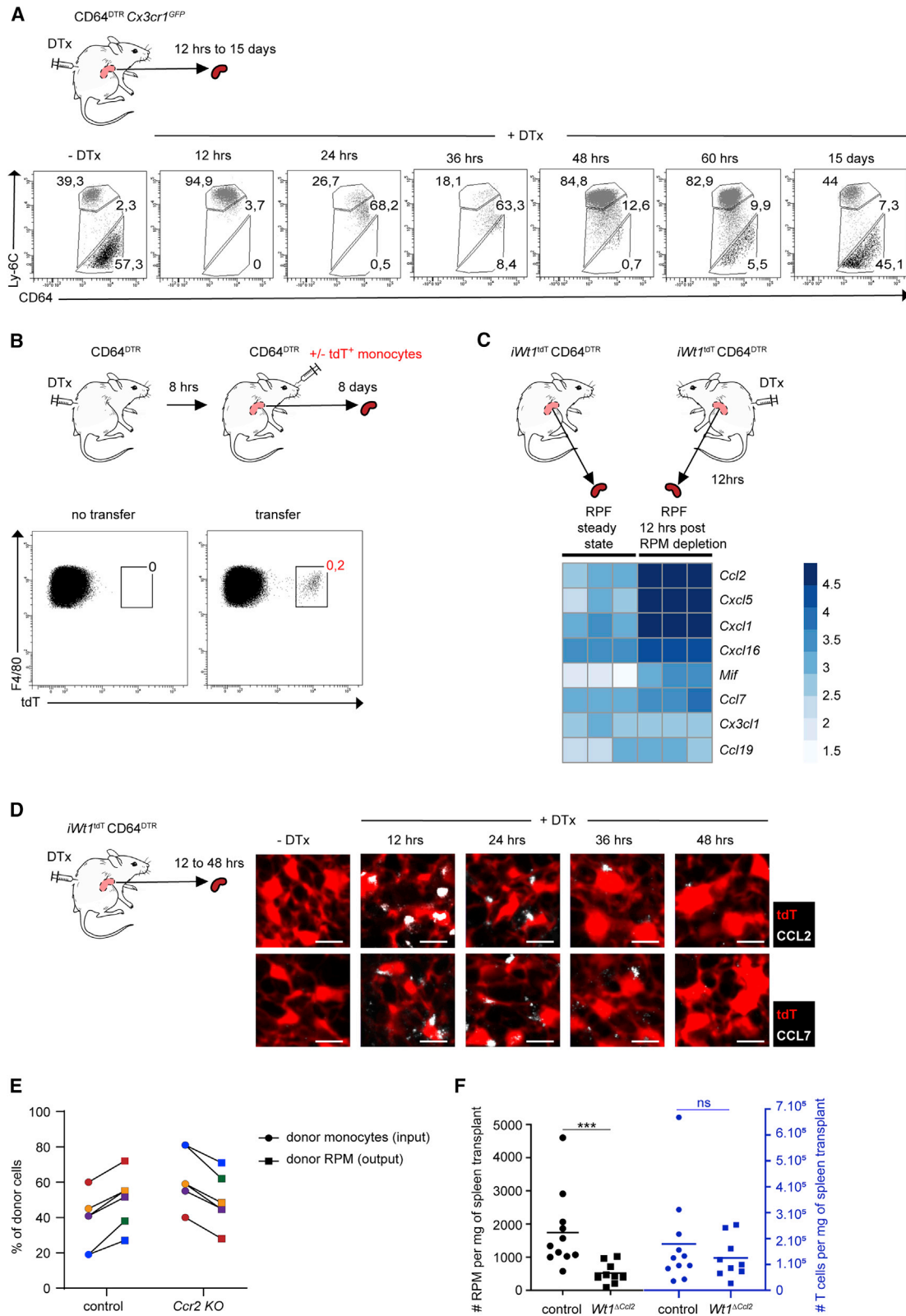


Figure 5. RP Fibroblasts Facilitate RPM Replenishment

(A) Adult *CD64^{DTR} Cx3cr1^{GFP/+}* mice were treated or not with DTx. Spleens were analyzed at the indicated time points by flow cytometry. Numbers indicate the percent of cells within *CD45⁺ CD11b⁺ F4/80⁺ GFP^{lo/-} MHCII^{lo}* myeloid pre-gated cells. Pooled data are from 2 independent experiments; n = 6 per time point.

(legend continued on next page)

gut, depleted macrophages are rapidly repopulated by circulating monocytes (Bain et al., 2014; Blériot et al., 2015; Lai et al., 2018; Mondor et al., 2019). Their recruitment relies on the secretion of a specific set of chemokines by the affected tissues (Shi and Pamer, 2011). We reasoned that in addition to their nurturing function, RP fibroblasts might actively produce these monocyte chemoattractants to replenish RPMs. This was tested by different and complementary approaches. We first took advantage of *Fcgr1* (CD64)^{DTR} mice in which all tissue resident macrophages and monocytes express DTR and are thus susceptible to DTx-mediated deletion (Baranska et al., 2018). DTx injection in adult CD64^{DTR} mice induced rapid and drastic depletion of RPMs within 12 h (Figures 5A and S5B) and subsequent changes in the monocyte compartment. Upon DTx injection, Ly6C^{hi} splenic monocytes were transiently depleted and a population of Ly6C^{int} monocytes appeared 24 h after DTx, eventually resembling mature RPMs (Ly6C^{lo/neg} CD64^{hi}) at 60 h. DTx treatment in wild-type (Wt) mice did not induce RPM deletion (Figure S5C). These data suggest that after RPM deletion, splenic and recruited monocytes gradually differentiated toward RPMs to repopulate their empty niche. To directly test this hypothesis, we delivered tdT-expressing monocytes to DTx-injected CD64^{DTR} mice. In line with previous work, labeled RPMs could be detected 8 days later, demonstrating that monocytes can contribute to the reconstitution of the RPM network (Figure 5B and Haldar et al., 2014). We then sought to determine whether RP fibroblasts actively participated in monocyte recruitment and the replenishment of the RPM network. To this aim, we first compared the transcriptome of steady-state RP fibroblasts to that of RP fibroblasts isolated from CD64^{DTR} mice injected with DTx 12 h before. We reasoned that this would be an ideal time point for the niche to call for monocytes, because RPMs were fully depleted. Bulk RNA-seq analysis revealed that RP fibroblasts isolated from mice depleted of RPMs were indeed enriched for transcripts encoding monocyte chemoattractants, such as *Ccl2* and *Ccl7* (Figure 5C). Immunostainings performed in tamoxifen-treated *iWt1*^{tdT} CD64^{DTR} mice confirmed that CCL2 and CCL7 protein abundantly colocalized with RP fibroblasts 12 h after DTx injection but were absent at steady state (Figure 5D). Neither CCL2 nor CCL7 were induced in Wt mice treated with DTx (not shown). This production lasted 48 h and coincided with the recruitment of high numbers of monocytes to the spleen (Figures 5A and 5D). We then investigated the role of these chemokines in the replenishment of the RPM network by two com-

plementary approaches. As monocytes sense the presence of both CCL2 and CCL7 via CCR2 (Kurihara and Bravo, 1996), we treated CD64^{DTR} mice with DTx and injected them i.v. with a mixture of wild-type and *Ccr2*-deficient monocytes bearing distinct fluorescent labels. Six days later, the contribution of the two types of monocytes to the replenishment of the RPM network was determined by imaging. In this set-up, *Ccr2*-deficient monocytes were consistently less competitive than their wild-type counterparts in giving rise to RPMs (Figures 5E and S5D). We then assessed the role of RP-fibroblast-derived CCL2 in the replenishment of RPMs by using a novel splenic organ graft model. Inguinal lymph nodes of Ubiquitin GFP (*Ubc*^{GFP}) mice were removed, and splenic fragments of a wild-type mouse were grafted in the empty inguinal pockets. Two months later, the grafted fragments were analyzed by flow cytometry (Figure S5E). We determined that host-derived GFP⁺ RPMs had abundantly (~60%) populated the splenic fragments. In order to assess the contribution of RP-fibroblast-derived CCL2 to RPM replenishment, we generated *Wt1*^{cre} mice bearing conditional alleles of *Ccl2* (*Wt1*^{ΔCcl2}). Wild-type and *Wt1*^{ΔCcl2} fragments were respectively grafted in the left and right inguinal pockets of *Ubc*^{GFP} recipients and analyzed 3 weeks later by flow cytometry (Figure 5F). Host and donor T cells were equally able to migrate to both spleen fragments. On the contrary, 68% less RPMs were recovered from *Wt1*^{ΔCcl2} fragments, suggesting that RP-fibroblast-derived CCL2 played an active role in recruiting monocytes. Altogether, our data point to RP fibroblasts representing master regulators of RPM biology via their ability to sustain RPM homeostasis and their capacity to replenish a damaged RPM network. Whether different or additional cues regulate the RPM niche during infection or inflammation remains to be investigated.

DISCUSSION

RPMs are key regulators of innate immune responses and iron metabolism (Kohyama et al., 2009; Kurotaki et al., 2015). Here we identified RP fibroblasts as central components of the cellular niche for RPMs, with roles in the maintenance of RPMs in homeostasis and their replenishment upon challenge.

A key function of the spleen is to recycle iron from senescent RBCs. To this aim, RPMs are strategically positioned within the RP cords, a labyrinthine structure in which blood circulation is open. *Wt1*^{ΔCsf1} mice developed iron overload in the splenic

(B) Adult CD64^{DTR} mice were treated with DTx and adoptively transferred with ~4.10⁶ tdT⁺ monocytes 8 h later. The percentage of tdT⁺ RPMs (0.241% ± 0.0234%) was determined 8 days later by flow cytometry. Data are representative of 2 independent experiments, n = 2 (no transfer) and n = 6 (transfer).

(C and D) Adult *iWt1*^{tdT} CD64^{DTR} mice were treated with tamoxifen. One week later, mice were treated or not with DTx.

(C) tdT-expressing RP fibroblasts were isolated 12 h later and analyzed by bulk RNA-seq for the expression of monocyte chemoattractant genes. Data show heatmap of normalized expression levels across replicates for selected genes.

(D) Spleens were stained for CCL2 and CCL7 protein at the indicated time points after DTx treatment. Data are representative of 2 independent experiments; n = 4. Scale bars, 10 μm.

(E) Adult CD64^{DTR} mice were treated with DTx. Eight hours later, mice were adoptively transferred with a mixture of ~4 to 8.10⁶ monocytes isolated from *Ccr2*^{WT} *Cx3cr1*^{GFP/+} *Ubc*^{tdT} and *Ccr2*^{KO} *Cx3cr1*^{GFP/+} adult mice. For each recipient, the percentages of injected *Ccr2*^{WT} and *Ccr2*^{KO} monocytes (input) as well as the percentages of *Ccr2*^{WT} and *Ccr2*^{KO} RPMs (output) recovered 6 days later were determined by flow cytometry and confocal imaging respectively. Each color corresponds to data from a single recipient. Data are representative of 2 independent experiments, n = 6. See also Figure S5D.

(F) Both inguinal lymph nodes were surgically removed from *Ubc*^{GFP} adult mice. Splenic fragments isolated from control or *Wt1*^{cre} mice bearing conditional alleles of *Ccl2* (*Wt1*^{ΔCcl2}) were grafted into the left and right inguinal pockets of *Ubc*^{GFP} recipients respectively. Three weeks later, the number of GFP⁺ donor-derived T cells and RPMs in both types of graft was determined by flow cytometry. Dots represent individual mice. Pooled data are from 2 independent experiments; n = 11 (control) and n = 9 (*Wt1*^{ΔCcl2}). Bars = means. See also Figure S5E.

RP, and transcriptomic analysis revealed that RP fibroblasts differ from FRCs in their limited expression of immune genes known to modulate T, B, and DCs and their strong enrichment in genes involved in the regulation of blood circulation. Based on this finding, we suggest that RP fibroblasts regulate iron metabolism by two complementary mechanisms. By providing CSF1 to RPMs and secreting monocyte chemoattractants upon RPM deletion, RP fibroblasts maintain a defined critical number of RBC-filtrating macrophages able to recycle hemoglobin iron. Whereas additional studies are required to investigate if and how they directly affect splenic blood flow, RP fibroblasts could modulate the influx of RBCs to the RP and thus ensure a steady supply of RBCs. The contractile nature of RP fibroblasts might also be particularly important during intense exercise, ischemic myocardial injury, or hemorrhages, when the spleen contracts to release RBCs, platelets, and monocytes stored in the RP (Baković et al., 2005; Greenway and Stark, 1969; Swirski et al., 2009).

It is currently thought that cellular niches not only nurture and anchor macrophages, but also “imprint” their identity in an active fashion by directly providing tissue-specific cues (Guilliams and Scott, 2017; Guilliams et al., 2020; T’Jonck et al., 2018). These regulate expression of key transcription factors in macrophages that in turn activate a population-specific genetic signature. In the peritoneal cavity for example, *Gata6* and *Cebpb* specify large peritoneal macrophages (Cain et al., 2013; Okabe and Medzhitov, 2014). In the bone, *Nfatc1* regulates osteoclast differentiation (Kim and Kim, 2014) whereas in the liver, *Id3* and *Lxra* control Kupffer cell identity (Bonnardel et al., 2019; Endo-Umeda et al., 2018; Mass et al., 2016; Sakai et al., 2019). As RPMs clear senescent RBCs from circulation, they are constantly exposed to heme, a toxic metabolite of hemoglobin degradation. Heme promotes monocyte differentiation into iron-recycling macrophages by inducing the expression of the transcription factor SPI-C, heme oxygenase 1 (*Hmox1*) and ferroportin (*Fpn1*) (Haldar et al., 2014; Kohyama et al., 2009). In *Spic*-deficient mice, RPMs can no longer protect themselves from toxic heme and are thus missing (Kohyama et al., 2009). Heme is a physiologic trigger of *Spic* induction, and feeding monocytes with heme is sufficient to induce *Spic* in these cells (Haldar et al., 2014). RP fibroblasts might thus indirectly confer RPM identity to incoming monocytes and resident RPMs by creating an anchoring meshwork wherein these cells constantly access heme-containing senescent RBCs, resulting in specification and maintenance of their genetic program. We propose that such “indirect imprinting” through physically providing access to specific tissue-derived cues represents a paradigm that is more globally applicable to the imprinting of tissue resident macrophages by efferocytic metabolites within their niche. In addition to this metabolic imprinting, additional transcription factors such as IRF4 and IRF8 are known to tailor RPM programming (Yamamoto et al., 2011). IRF8 is abundantly expressed in RPMs (Kurotaki et al., 2015) and is induced by TGF- β signaling (Humblin et al., 2017). In keeping with this, deletion of *Tgfb2* in hematopoietic cells results in a 50% decrease of the RPM population (Yu et al., 2017). We found that RP fibroblasts express TGF- β isoforms, suggesting that RP fibroblast might imprint RPM programming through TGF- β production and IRF8 induction.

It is highly conceivable that RP fibroblasts and RPMs engage in two-sided crosstalk. Medzhitov and colleagues predicted the

existence of two-cell circuits between fibroblasts and macrophages, in which the latter provide trophic factors to fibroblasts in return for survival cues, identifying the CSF1-CSF1R and PDGF-PDGFR axis as the minimal molecular language sustaining fibroblast-macrophage circuitry *in vitro* (Zhou et al., 2018). Although we found that RP fibroblasts indeed expressed PDGFR α and β , none of the members of the PDGF ligand family are expressed significantly by RPMs. Our analysis of RPMs and RP fibroblast transcriptomes revealed two pairs of ligand-receptors that could positively influence RP fibroblasts: TNFR-GRN and TGF β R3-TGF β 1. *Tnfrsf1a* and *b* (encoding tumor necrosis factor receptor types I and II) and *Gm* (Progranulin) were expressed at high levels by RP fibroblasts and RPMs, respectively. GRN binds to TNFR and suppresses TNF α signaling while also acting as a survival and growth factor for fibroblasts during wound repair (He et al., 2003; Tang et al., 2011; Zanocco-Marani et al., 1999). TGF β R3 (transforming growth factor beta receptor 3 or Betaglycan) and one of its ligands, TGF β 1, were also expressed by RP fibroblasts and RPMs, respectively (Kurotaki et al., 2011). TGF β signaling regulates cell proliferation, differentiation, communication, adhesion, movement, metabolism, and death in many cell types, including fibroblasts (David and Massagué, 2018). Betaglycan is a co-receptor for TGF β that establishes the potency of its ligands to their target cells (López-Casillas et al., 1991). Interestingly, deletion of *Tgfb2* in fibroblasts induces expression of CCL2 in a mammary tumor model, suggesting that TGF β signaling in RP fibroblasts might control their homeostasis as well as their ability to recruit monocytes in the absence of TGF β -producing RPMs (Fang et al., 2011). Additional experiments will be required to unravel the molecular dialog established between RPMs and RP fibroblasts.

CSF1 regulates macrophage homeostasis across tissues and is expressed by various cell types, including endothelial cells and fibroblasts (Mondor et al., 2019). The molecular mechanisms regulating expression of macrophage survival factors such as CSF1 in stromal cell types is incompletely understood. Is there a core set of genes conferring a “macrophage niche” program in different cell types such as LECs and RP fibroblasts? There is some evidence suggesting that transcription factors might instruct macrophage niches. The transcription factor GATA6 controls the homeostasis and metabolism of peritoneal cavity-resident macrophages, and its expression is induced by retinoic acid. WT1 drives the expression of two rate-limiting enzymes in retinol metabolism: *Raldh1* and *Raldh2* (Buechler et al., 2019). By using various mouse models and *in vitro* studies, Buechler et al. identified retinol-producing WT1-expressing stromal cells as a niche imprinting large cavity-resident macrophages. WT1 is a multifaceted protein that regulates gene expression both at the transcriptional and post-transcriptional levels (Hastie, 2017). Interestingly, endogenous WT1 interacts with *Csf1* transcripts, thus possibly regulating their stability (Bharathavikru et al., 2017). WT1 also binds genes belonging to the laminin, collagen, and integrin families, some of which are expressed by RP fibroblasts (*Lamb2*, *Lama5*, *Lamc1*, *Col18a1*, *Col1a2*; Figure S1B). In lung fibroblasts, WT1 is associated with positive regulation of *Nt5e* and *Vcam1* (Sontake et al., 2018), two genes that are also expressed by RP fibroblasts. Furthermore, it has been suggested that WT1 and the transcription factor TCF21 cooperatively control the specification of glomerular podocytes. As

Tcsf21^{CreERT2} mice fate map a population of splenic RP reticular cells (Inra et al., 2015), it is conceivable that WT1 and TCF21 also cooperate to program RP fibroblasts in the spleen, another blood filtering organ.

Adding a further layer of complexity, CSF1 is expressed as membrane-bound and soluble isoforms (Chitu and Stanley, 2006). Stanley et al. engineered a transgenic mouse in which the membrane-bound isoform of CSF1 was reintroduced to normal levels into otherwise *Csf1*-deficient (*Csf1*^{op/op}) mice (Dai et al., 2004). Although these mice had no detectable CSF1 in their blood, the gross defects associated with the *Csf1*^{op/op} genotype, including the paucity of most macrophage populations, were corrected (Dai et al., 2004). These results suggest that the majority of tissue-resident macrophage relies upon a membrane-bound source of CSF1 provided locally by their cellular niches. Our results are consistent with this hypothesis. Although blood levels of CSF1 were normal in *Wt1*^{ΔCsf1} mice, RPMs and large cavity macrophages were reduced in these mice, suggesting that circulating levels of CSF1 are insufficient to sustain the homeostasis of these macrophages. Why would macrophage niches favor the production of membrane-bound CSF1? The soluble isoform of CSF1 is very potent to sustain macrophage survival *in vitro* and *in vivo*. Injection of soluble CSF1 in *Csf1*^{op/op} mice rescues most macrophage subsets including RPMs (Cecchini et al., 1994). In support of this notion, we found that 25% of RPMs remained in the spleen of *Wt1*^{ΔCsf1} mice despite complete deletion of *Csf1* in RP fibroblasts. In theory, macrophage homeostasis could thus be regulated by either isoform, and at first sight, one might argue that the soluble form should be favorable for macrophage populations with direct access to the circulation, such as RPMs. However, we would argue that their dependence on the membrane-bound isoform of CSF1 represents the best option to locally nurture these abundant macrophages without more globally affecting macrophages in other organs and other blood-filtering macrophages such as liver Kupffer cells in particular. Membrane-bound CSF1 might also be imperative for the establishment of two-cell circuits between macrophages and their niche, because it would facilitate continuous delivery of macrophage-derived homeostatic signals, a hypothesis that remains to be tested experimentally *in vivo*.

Altogether, we have identified the cellular and molecular mechanisms regulating the homeostasis and replenishment of RPMs, the most abundant population of splenic macrophages that exert a major role in iron metabolism. We characterized a population of splenic RP stromal cells as CSF1-producing fibroblasts and identified these as a key component of the RPM niche.

LIMITATIONS OF THE STUDY

A limitation of our study is that we identified RP fibroblasts as regulators of RPM replenishment after genetic perturbation of their network but did not address this in additional, pathophysiologically relevant conditions such as infections. However, macrophage deletion is almost invariably accompanied by an inflammatory process. We thus cannot envision situations in which RPM deletion would not also be associated with inflammation and consider it very likely that RP fibroblasts would be equally involved in RPM replenishment in inflammatory or infectious conditions. For the same reason, we believe it would be technically

challenging to decipher the precise mechanism(s) governing the production of monocyte chemoattractants by RP fibroblasts after RPM depletion. This production could result from two non-mutually mechanisms, which we acknowledge have not been explored in this study. RP fibroblasts and RPMs might physically interact via an unknown mechanism that continuously represses CCL2 and CCL7 production. Upon RPM deletion, this inhibition would be removed, allowing monocyte recruitment. The newly recruited monocyte would settle in the vacant niche and re-establish this inhibitory bond, ensuring that no further monocytes would be recruited to this niche. Alternatively, RP fibroblasts could be actively induced to secrete CCL2 and CCL7 in response to the inflammation triggered by the synchronous and massive death of RPMs. Regardless of the relative contribution of these mechanisms, RP fibroblasts would actively participate in RPM replenishment in either scenario. Our data demonstrated that RP fibroblasts maintain RPM homeostasis directly via the provision of CSF1. Whether RPM loss in *Wt1*^{ΔCsf1} mice is due to cell death or emigration of RPMs from the spleen remains to be investigated.

Our study also highlights limitations of conditional mouse models. Ideally, conditional deletion of *Csf1* should have been also performed in *Wt1*^{CreERT2} Rosa^{tdT} (*iWt1*^{tdT}) mice in order to bypass any developmental defect associated with the constitutive deletion of *Csf1* occurring in *Wt1*^{ΔCsf1} mice. We have generated *iWt1*^{tdT ΔCsf1} mice but noticed that *Csf1* was not efficiently deleted in tdT⁺ RP fibroblasts after tamoxifen treatment, reinforcing the idea that fluorescent reporter mice should not be used as systemic proxies for gene deletion efficacy. Finally, the stromal cell field urgently needs to generate additional tools allowing reliable and efficient targeting of individual stroma cell subsets.

STAR★METHODS

Detailed methods are provided in the online version of this paper and include the following:

- KEY RESOURCES TABLE
- RESOURCE AVAILABILITY
 - Lead Contact
 - Materials Availability
 - Data and code availability
- EXPERIMENTAL MODEL AND SUBJECTS DETAILS
 - Mice
- METHOD DETAILS
 - Tamoxifen administration
 - Bone marrow chimeras
 - Isolation of RPM, splenic stromal cells, and lymph node FRC
 - Flow cytometry
 - Immunostaining for confocal microscopy
 - Iron Staining
 - Scanning Electron Microscopy
 - Antibodies
 - Diphtheria toxin mediated RPM or RP Fibroblasts depletion
 - Monocyte transfer
 - Spleen grafting
 - Bulk RNA Sequencing and bioinformatics analysis
 - Murine spleen scRNAseq data analysis

- Human spleen processing
- Human spleen scRNAseq analysis
- Dosage of serum CSF1
- qRT-PCR
- **QUANTIFICATION AND STATISTICAL ANALYSIS**
 - Quantification of YFP⁺ pixels in the Red Pulp
 - Quantification of cells
 - Statistical analysis

SUPPLEMENTAL INFORMATION

Supplemental Information can be found online at <https://doi.org/10.1016/j.immuni.2020.06.008>.

ACKNOWLEDGMENTS

We thank Andrea Brendolan (Ospedale San Raffaele, Milan, Italy) and Burkhard Ludewig (Institute of Immunobiology, Kantonsspital St. Gallen, Switzerland) for providing spleens of *Nkx2.5^{Cre} Rosa^{YFP}* mice and *Cc19^{Cre}* mice, respectively; the CIML core facilities for animal housing and flow cytometry; the ImagImm photonic microscopy facility of the Centre d'Immunologie de Marseille-Luminy; and Rebecca Gentek for critical comments on the manuscript. The electron microscopy experiments were performed at the Plateforme d'Imagerie Commune des Sites de Luminy–France BioImaging core facility (Institut de Biologie du Développement de Marseille, Aix-Marseille Université), a member of the France-BioImaging National Research Infrastructure. This study was funded by grants from the Agence National pour la Recherche (ANR-10-INBS-04-01 France Bio Imaging and ANR-17-CE15-0015-01), the Fondation pour la Recherche Médicale (FRM), and from the European Research Council (ERC) under the European Union's Horizon 2020 research and innovation program grant agreement 647257- STROMA. This work was supported by institutional grants from INSERM, CNRS, and Aix-Marseille University to the CIML. The authors declare no conflict of interest.

AUTHOR CONTRIBUTIONS

Conceptualization, A.B. and M.B.; Methodology, A.B., L.S., and M.B.; Investigation, A.B., I.M., L.S., M.L., B.B., N.B., M.N., and M.B.; Resources, B.M., L.S., and M.N.; Writing, A.B. and M.B.; Supervision, M.B.; Project Administration, M.B.; Funding Acquisition, M.B.

DECLARATION OF INTERESTS

The authors declare no competing interests

Received: October 18, 2019
Revised: March 20, 2020
Accepted: June 4, 2020
Published: June 19, 2020

REFERENCES

A-Gonzalez, N., and Castrillo, A. (2018). Origin and specialization of splenic macrophages. *Cell. Immunol.* **330**, 151–158.

Acton, S.E., Farrugia, A.J., Astarita, J.L., Mourão-Sá, D., Jenkins, R.P., Nye, E., Hooper, S., van Blijswijk, J., Rogers, N.C., Snelgrove, K.J., et al. (2014). Dendritic cells control fibroblastic reticular network tension and lymph node expansion. *Nature* **514**, 498–502.

Aibar, S., González-Bias, C.B., Moerman, T., Huynh-Thu, V.A., Imrichova, H., Hulselmans, G., Rambow, F., Marine, J.C., Geurts, P., Aerts, J., et al. (2017). SCENIC: single-cell regulatory network inference and clustering. *Nat. Methods* **14**, 1083–1086.

Astarita, J.L., Cremasco, V., Fu, J., Darnell, M.C., Peck, J.R., Nieves-Bonilla, J.M., Song, K., Kondo, Y., Woodruff, M.C., Gogineni, A., et al. (2015). The CLEC-2-podoplanin axis controls the contractility of fibroblastic reticular cells and lymph node microarchitecture. *Nat. Immunol.* **16**, 75–84.

Bain, C.C., Bravo-Blas, A., Scott, C.L., Perdiguero, E.G., Geissmann, F., Henri, S., Malissen, B., Osborne, L.C., Artis, D., and Mowat, A.M. (2014). Constant replenishment from circulating monocytes maintains the macrophage pool in the intestine of adult mice. *Nat. Immunol.* **15**, 929–937.

Baković, D., Eterović, D., Saratlija-Novaković, Z., Palada, I., Valic, Z., Bilopavlović, N., and Dujic, Z. (2005). Effect of human splenic contraction on variation in circulating blood cell counts. *Clin. Exp. Pharmacol. Physiol.* **32**, 944–951.

Baranska, A., Shawket, A., Jouve, M., Baratin, M., Malosse, C., Voluzan, O., Vu Manh, T.P., Fiore, F., Bajénoff, M., Benaroch, P., et al. (2018). Unveiling skin macrophage dynamics explains both tattoo persistence and strenuous removal. *J. Exp. Med.* **215**, 1115–1133.

Baratin, M., Simon, L., Jorquera, A., Ghigo, C., Dembele, D., Nowak, J., Gentek, R., Wiernert, S., Klauschen, F., Malissen, B., et al. (2017). T Cell Zone Resident Macrophages Silently Dispose of Apoptotic Cells in the Lymph Node. *Immunity* **47**, 349–362.e5, e345.

Bharathavikru, R., Dudnakova, T., Aitken, S., Slight, J., Artibani, M., Hohenstein, P., Tollervey, D., and Hastie, N. (2017). Transcription factor Wilms' tumor 1 regulates developmental RNAs through 3' UTR interaction. *Genes Dev.* **31**, 347–352.

Bhattacharya, S., Dunn, P., Thomas, C.G., Smith, B., Schaefer, H., Chen, J., Hu, Z., Zalocusky, K.A., Shankar, R.D., Shen-Orr, S.S., et al. (2018). ImmPort, toward repurposing of open access immunological assay data for translational and clinical research. *Sci. Data* **5**, 180015.

Blériot, C., Dupuis, T., Jouvion, G., Eberl, G., Disson, O., and Lecuit, M. (2015). Liver-resident macrophage necroptosis orchestrates type 1 microbicidal inflammation and type-2-mediated tissue repair during bacterial infection. *Immunity* **42**, 145–158.

Bonnardel, J., T'Jonck, W., Gaublomme, D., Browaeys, R., Scott, C.L., Martens, L., Vanneste, B., De Prijck, S., Nedospasov, S.A., Kremer, A., et al. (2019). Stellate Cells, Hepatocytes, and Endothelial Cells Imprint the Kupffer Cell Identity on Monocytes Colonizing the Liver Macrophage Niche. *Immunity* **51**, 638–654.e9.

Boring, L., Gosling, J., Chensue, S.W., Kunkel, S.L., Farese, R.V., Jr., Broxmeyer, H.E., and Charo, I.F. (1997). Impaired monocyte migration and reduced type 1 (Th1) cytokine responses in C-C chemokine receptor 2 knockout mice. *J. Clin. Invest.* **100**, 2552–2561.

Buch, T., Heppner, F.L., Tertilt, C., Heinen, T.J., Kremer, M., Wunderlich, F.T., Jung, S., and Waisman, A. (2005). A Cre-inducible diphtheria toxin receptor mediates cell lineage ablation after toxin administration. *Nat. Methods* **2**, 419–426.

Buechler, M.B., Kim, K.W., Onufer, E.J., Williams, J.W., Little, C.C., Dominguez, C.X., Li, Q., Sandoval, W., Cooper, J.E., Harris, C.A., et al. (2019). A Stromal Niche Defined by Expression of the Transcription Factor WT1 Mediates Programming and Homeostasis of Cavity-Resident Macrophages. *Immunity* **51**, 119–130.e5.

Cain, D.W., O'Koren, E.G., Kan, M.J., Womble, M., Sempowski, G.D., Hopper, K., Gunn, M.D., and Kelsoe, G. (2013). Identification of a tissue-specific, C/EBP β -dependent pathway of differentiation for murine peritoneal macrophages. *J. Immunol.* **191**, 4665–4675.

Camara, A., Cordeiro, O.G., Alloush, F., Sponsel, J., Chypre, M., Onder, L., Asano, K., Tanaka, M., Yagita, H., Ludewig, B., et al. (2019). Lymph Node Mesenchymal and Endothelial Stromal Cells Cooperate via the RANK-RANKL Cytokine Axis to Shape the Sinusoidal Macrophage Niche. *Immunity* **50**, 1467–1481.e6, e1466.

Castagnaro, L., Lenti, E., Maruzzelli, S., Spinardi, L., Migliori, E., Farinello, D., Sitia, G., Harrelson, Z., Evans, S.M., Guidotti, L.G., et al. (2013). Nkx2-5(+) islet1(+) mesenchymal precursors generate distinct spleen stromal cell subsets and participate in restoring stromal network integrity. *Immunity* **38**, 782–791.

Cecchini, M.G., Dominguez, M.G., Mocci, S., Wetterwald, A., Felix, R., Fleisch, H., Chisholm, O., Hofstetter, W., Pollard, J.W., and Stanley, E.R. (1994). Role of colony stimulating factor-1 in the establishment and regulation of tissue macrophages during postnatal development of the mouse. *Development* **120**, 1357–1372.

- Chai, Q., Onder, L., Scandella, E., Gil-Cruz, C., Perez-Shibayama, C., Cupovic, J., Danuser, R., Sparwasser, T., Luther, S.A., Thiel, V., et al. (2013). Maturation of lymph node fibroblastic reticular cells from myofibroblastic precursors is critical for antiviral immunity. *Immunity* 38, 1013–1024.
- Chau, Y.Y., Brownstein, D., Mjoseng, H., Lee, W.C., Buza-Vidas, N., Nerlov, C., Jacobsen, S.E., Perry, P., Berry, R., Thornburn, A., et al. (2011). Acute multiple organ failure in adult mice deleted for the developmental regulator *Wt1*. *PLoS Genet.* 7, e1002404.
- Chen, L.T., and Weiss, L. (1972). Electron microscopy of the red pulp of human spleen. *Am. J. Anat.* 734, 425–457.
- Cheng, H.W., Onder, L., Novkovic, M., Soneson, C., Lütge, M., Pikor, N., Scandella, E., Robinson, M.D., Miyazaki, J.I., Tersteegen, A., et al. (2019). Origin and differentiation trajectories of fibroblastic reticular cells in the splenic white pulp. *Nat. Commun.* 10, 1739.
- Chitu, V., and Stanley, E.R. (2006). Colony-stimulating factor-1 in immunity and inflammation. *Curr. Opin. Immunol.* 18, 39–48.
- Coelho, F.M., Natale, D., Soriano, S.F., Hons, M., Swoger, J., Mayer, J., Danuser, R., Scandella, E., Pieczyk, M., Zerwes, H.G., et al. (2013). Naive B-cell trafficking is shaped by local chemokine availability and LFA-1-independent stromal interactions. *Blood* 121, 4101–4109.
- Dai, X.M., Ryan, G.R., Hapel, A.J., Dominguez, M.G., Russell, R.G., Kapp, S., Sylvestre, V., and Stanley, E.R. (2002). Targeted disruption of the mouse colony-stimulating factor 1 receptor gene results in osteopetrosis, mononuclear phagocyte deficiency, increased primitive progenitor cell frequencies, and reproductive defects. *Blood* 99, 111–120.
- Dai, X.M., Zong, X.H., Sylvestre, V., and Stanley, E.R. (2004). Incomplete restoration of colony-stimulating factor 1 (CSF-1) function in CSF-1-deficient *Csf1op/Csf1op* mice by transgenic expression of cell surface CSF-1. *Blood* 103, 1114–1123.
- David, C.J., and Massagué, J. (2018). Contextual determinants of TGF β action in development, immunity and cancer. *Nat. Rev. Mol. Cell Biol.* 19, 419–435.
- DeFalco, T., Potter, S.J., Williams, A.V., Waller, B., Kan, M.J., and Capel, B. (2015). Macrophages Contribute to the Spermatogonial Niche in the Adult Testis. *Cell Rep.* 12, 1107–1119.
- Egen, J.G., Rothfuchs, A.G., Feng, C.G., Winter, N., Sher, A., and Germain, R.N. (2008). Macrophage and T cell dynamics during the development and disintegration of mycobacterial granulomas. *Immunity* 28, 271–284.
- Endo-Umeda, K., Nakashima, H., Komine-Aizawa, S., Umeda, N., Seki, S., and Makishima, M. (2018). Liver X receptors regulate hepatic F4/80⁺ CD11b⁺ Kupffer cells/macrophages and innate immune responses in mice. *Sci. Rep.* 8, 9281.
- Epelman, S., Lavine, K.J., Beaudin, A.E., Sojka, D.K., Carrero, J.A., Calderon, B., Brija, T., Gautier, E.L., Ivanov, S., Satpathy, A.T., et al. (2014). Embryonic and adult-derived resident cardiac macrophages are maintained through distinct mechanisms at steady state and during inflammation. *Immunity* 40, 91–104.
- Fang, W.B., Jokar, I., Chytil, A., Moses, H.L., Abel, T., and Cheng, N. (2011). Loss of one *Tgfb2* allele in fibroblasts promotes metastasis in MMTV: polyoma middle T transgenic and transplant mouse models of mammary tumor progression. *Clin. Exp. Metastasis* 28, 351–366.
- Feyerabend, T.B., Weiser, A., Tietz, A., Stassen, M., Harris, N., Kopf, M., Radermacher, P., Möller, P., Benoist, C., Mathis, D., et al. (2011). Cre-mediated cell ablation contests mast cell contribution in models of antibody- and T cell-mediated autoimmunity. *Immunity* 35, 832–844.
- Ghigo, C., Mondor, I., Jorquera, A., Nowak, J., Wienert, S., Zahner, S.P., Clausen, B.E., Luche, H., Malissen, B., Klauschen, F., and Bajénoff, M. (2013). Multicolor fate mapping of Langerhans cell homeostasis. *J. Exp. Med.* 210, 1657–1664.
- Golub, R., Tan, J., Watanabe, T., and Brendolan, A. (2018). Origin and Immunological Functions of Spleen Stromal Cells. *Trends Immunol.* 39, 503–514.
- Greenway, C.V., and Stark, R.D. (1969). Vascular responses of the spleen to rapid haemorrhage in the anaesthetized cat. *J. Physiol.* 204, 169–179.
- Greter, M., Lelios, I., Pelczar, P., Hoeffel, G., Price, J., Leboeuf, M., Kündig, T.M., Frei, K., Ginhoux, F., Merad, M., and Becher, B. (2012). Stroma-derived interleukin-34 controls the development and maintenance of langerhans cells and the maintenance of microglia. *Immunity* 37, 1050–1060.
- Guilliams, M., and Scott, C.L. (2017). Does niche competition determine the origin of tissue-resident macrophages? *Nat. Rev. Immunol.* 17, 451–460.
- Guilliams, M., Thierry, G.R., Bonnardel, J., and Bajénoff, M. (2020). Establishment and Maintenance of the Macrophage Niche. *Immunity* 52, 434–451.
- Haghverdi, L., Lun, A.T.L., Morgan, M.D., and Marioni, J.C. (2018). Batch effects in single-cell RNA-sequencing data are corrected by matching mutual nearest neighbors. *Nat. Biotechnol.* 36, 421–427.
- Haldar, M., Kohyama, M., So, A.Y., Kc, W., Wu, X., Briseño, C.G., Satpathy, A.T., Kretzer, N.M., Arase, H., Rajasekaran, N.S., et al. (2014). Heme-mediated SPI-C induction promotes monocyte differentiation into iron-recycling macrophages. *Cell* 156, 1223–1234.
- Hara, T., Katakai, T., Lee, J.H., Nambu, Y., Nakajima-Nagata, N., Gonda, H., Sugai, M., and Shimizu, A. (2006). A transmembrane chemokine, CXC chemokine ligand 16, expressed by lymph node fibroblastic reticular cells has the potential to regulate T cell migration and adhesion. *Int. Immunol.* 18, 301–311.
- Harris, S.E., MacDougall, M., Horn, D., Woodruff, K., Zimmer, S.N., Rebel, V.I., Fajardo, R., Feng, J.Q., Gluhak-Heinrich, J., Harris, M.A., and Abboud Werner, S. (2012). *Meox2*Cre-mediated disruption of CSF-1 leads to osteopetrosis and osteocyte defects. *Bone* 50, 42–53.
- Hashimoto, D., Chow, A., Noizat, C., Teo, P., Beasley, M.B., Leboeuf, M., Becker, C.D., See, P., Price, J., Lucas, D., et al. (2013). Tissue-resident macrophages self-maintain locally throughout adult life with minimal contribution from circulating monocytes. *Immunity* 38, 792–804.
- Hastie, N.D. (2017). Wilms' tumour 1 (WT1) in development, homeostasis and disease. *Development* 144, 2862–2872.
- He, Z., Ong, C.H., Halper, J., and Bateman, A. (2003). Progranulin is a mediator of the wound response. *Nat. Med.* 9, 225–229.
- Humblin, E., Thibaudin, M., Chalmin, F., Derangère, V., Limagne, E., Richard, C., Flavell, R.A., Chevrier, S., Ladoire, S., Berger, H., et al. (2017). IRF8-dependent molecular complexes control the Th9 transcriptional program. *Nat. Commun.* 8, 2085.
- Inra, C.N., Zhou, B.O., Acar, M., Murphy, M.M., Richardson, J., Zhao, Z., and Morrison, S.J. (2015). A perisinusoidal niche for extramedullary haematopoiesis in the spleen. *Nature* 527, 466–471.
- Jarjour, M., Jorquera, A., Mondor, I., Wienert, S., Narang, P., Coles, M.C., Klauschen, F., and Bajénoff, M. (2014). Fate mapping reveals origin and dynamics of lymph node follicular dendritic cells. *J. Exp. Med.* 211, 1109–1122.
- Jung, S., Aliberti, J., Graemmel, P., Sunshine, M.J., Kreutzberg, G.W., Sher, A., and Littman, D.R. (2000). Analysis of fractalkine receptor CX3CR1 function by targeted deletion and green fluorescent protein reporter gene insertion. *Mol. Cell. Biol.* 20, 4106–4114.
- Katakai, T., Suto, H., Sugai, M., Gonda, H., Togawa, A., Suematsu, S., Ebisuno, Y., Katagiri, K., Kinashi, T., and Shimizu, A. (2008). Organizer-like reticular stromal cell layer common to adult secondary lymphoid organs. *J. Immunol.* 181, 6189–6200.
- Kim, J.H., and Kim, N. (2014). Regulation of NFATc1 in Osteoclast Differentiation. *J. Bone Metab.* 21, 233–241.
- Kim, J., Prawitt, D., Bardeesy, N., Torban, E., Vicaner, C., Goodyer, P., Zabel, B., and Pelletier, J. (1999). The Wilms' tumor suppressor gene (*wt1*) product regulates *Dax-1* gene expression during gonadal differentiation. *Mol. Cell. Biol.* 19, 2289–2299.
- Kohyama, M., Ise, W., Edelson, B.T., Wilker, P.R., Hildner, K., Mejia, C., Frazier, W.A., Murphy, T.L., and Murphy, K.M. (2009). Role for Spi-C in the development of red pulp macrophages and splenic iron homeostasis. *Nature* 457, 318–321.
- Kurihara, T., and Bravo, R. (1996). Cloning and functional expression of mCCR2, a murine receptor for the C-C chemokines JE and FIC. *J. Biol. Chem.* 271, 11603–11607.
- Kurotaki, D., Kon, S., Bae, K., Ito, K., Matsui, Y., Nakayama, Y., Kanayama, M., Kimura, C., Narita, Y., Nishimura, T., et al. (2011). CSF-1-dependent red pulp macrophages regulate CD4 T cell responses. *J. Immunol.* 186, 2229–2237.

- Kurotaki, D., Uede, T., and Tamura, T. (2015). Functions and development of red pulp macrophages. *Microbiol. Immunol.* **59**, 55–62.
- Lai, S.M., Sheng, J., Gupta, P., Renia, L., Duan, K., Zolezzi, F., Karjalainen, K., Newell, E.W., and Ruedl, C. (2018). Organ-Specific Fate, Recruitment, and Refilling Dynamics of Tissue-Resident Macrophages during Blood-Stage Malaria. *Cell Rep.* **25**, 3099–3109.e3, e3093.
- Lavin, Y., Mortha, A., Rahman, A., and Merad, M. (2015). Regulation of macrophage development and function in peripheral tissues. *Nat. Rev. Immunol.* **15**, 731–744.
- Lin, W., Xu, D., Austin, C.D., Caplazi, P., Senger, K., Sun, Y., Jeet, S., Young, J., Delarosa, D., Suto, E., et al. (2019). Function of CSF1 and IL34 in Macrophage Homeostasis, Inflammation, and Cancer. *Front. Immunol.* **10**, 2019.
- Link, A., Vogt, T.K., Favre, S., Britschgi, M.R., Acha-Orbea, H., Hinz, B., Cyster, J.G., and Luther, S.A. (2007). Fibroblastic reticular cells in lymph nodes regulate the homeostasis of naive T cells. *Nat. Immunol.* **8**, 1255–1265.
- López-Casillas, F., Cheifetz, S., Doody, J., Andres, J.L., Lane, W.S., and Massagué, J. (1991). Structure and expression of the membrane proteoglycan betaglycan, a component of the TGF-beta receptor system. *Cell* **67**, 785–795.
- Luche, H., Weber, O., Nageswara Rao, T., Blum, C., and Fehling, H.J. (2007). Faithful activation of an extra-bright red fluorescent protein in “knock-in” Cre-reporter mice ideally suited for lineage tracing studies. *Eur. J. Immunol.* **37**, 43–53.
- Madisen, L., Zwingman, T.A., Sunkin, S.M., Oh, S.W., Zariwala, H.A., Gu, H., Ng, L.L., Palmiter, R.D., Hawrylycz, M.J., Jones, A.R., et al. (2010). A robust and high-throughput Cre reporting and characterization system for the whole mouse brain. *Nat. Neurosci.* **13**, 133–140.
- Malhotra, D., Fletcher, A.L., Astarita, J., Lukacs-Kornek, V., Tayalia, P., Gonzalez, S.F., Elpek, K.G., Chang, S.K., Knoblich, K., Hemler, M.E., et al.; Immunological Genome Project Consortium (2012). Transcriptional profiling of stroma from inflamed and resting lymph nodes defines immunological hallmarks. *Nat. Immunol.* **13**, 499–510.
- Mass, E., Ballesteros, I., Farlik, M., Halbritter, F., Günther, P., Crozet, L., Jacome-Galarza, C.E., Händler, K., Klughammer, J., Kobayashi, Y., et al. (2016). Specification of tissue-resident macrophages during organogenesis. *Science* **353**, 353.
- Mebius, R.E., and Kraal, G. (2005). Structure and function of the spleen. *Nat. Rev. Immunol.* **5**, 606–616.
- Medina-Contreras, O., Geem, D., Laur, O., Williams, I.R., Lira, S.A., Nusrat, A., Parkos, C.A., and Denning, T.L. (2011). CX3CR1 regulates intestinal macrophage homeostasis, bacterial translocation, and colitogenic Th17 responses in mice. *J. Clin. Invest.* **121**, 4787–4795.
- Melsted, P., Ntranos, V., and Pachter, L. (2019). The barcode, UMI, set format and BUSTools. *Bioinformatics* **35**, 4472–4473.
- Mondor, I., Baratin, M., Laguerie, M., Saro, L., Henri, S., Gentek, R., Suerinck, D., Kastenmuller, W., Jiang, J.X., and Bajénoff, M. (2019). Lymphatic Endothelial Cells Are Essential Components of the Subcapsular Sinus Macrophage Niche. *Immunity* **50**, 1453–1466.e4, e1454.
- Mueller, S.N., and Germain, R.N. (2009). Stromal cell contributions to the homeostasis and functionality of the immune system. *Nat. Rev. Immunol.* **9**, 618–629.
- Okabe, Y., and Medzhitov, R. (2014). Tissue-specific signals control reversible program of localization and functional polarization of macrophages. *Cell* **157**, 832–844.
- Okada, T., and Cyster, J.G. (2007). CC chemokine receptor 7 contributes to Gi-dependent T cell motility in the lymph node. *J. Immunol.* **178**, 2973–2978.
- Robinson, N., McComb, S., Mulligan, R., Dudani, R., Krishnan, L., and Sad, S. (2012). Type I interferon induces necroptosis in macrophages during infection with *Salmonella enterica* serovar Typhimurium. *Nat. Immunol.* **13**, 954–962.
- Rubin, J., Fan, X., Thornton, D., Bryant, R., and Biskobing, D. (1996). Regulation of murine osteoblast macrophage colony-stimulating factor production by 1,25(OH)₂D₃. *Calcified tissue international* **59**, 291–296.
- Sakai, M., Troutman, T.D., Seidman, J.S., Ouyang, Z., Spann, N.J., Abe, Y., Ego, K.M., Bruni, C.M., Deng, Z., Schlachetzki, J.C.M., et al. (2019). Liver-Derived Signals Sequentially Reprogram Myeloid Enhancers to Initiate and Maintain Kupffer Cell Identity. *Immunity* **51**, 655–670.e8.
- Schneider, C., Nobs, S.P., Heer, A.K., Kurrer, M., Klinke, G., van Rooijen, N., Vogel, J., and Kopf, M. (2014). Alveolar macrophages are essential for protection from respiratory failure and associated morbidity following influenza virus infection. *PLoS Pathog.* **10**, e1004053.
- Schneider, C.A., Rasband, W.S., and Eliceiri, K.W. (2012). NIH Image to ImageJ: 25 years of image analysis. *Nat. Methods* **9**, 671–675.
- Shi, C., and Pamer, E.G. (2011). Monocyte recruitment during infection and inflammation. *Nat. Rev. Immunol.* **11**, 762–774.
- Smedley, D., Haider, S., Ballester, B., Holland, R., London, D., Thorisson, G., and Kasprzyk, A. (2009). BioMart—biological queries made easy. *BMC Genomics* **10**, 22.
- Sontake, V., Kasam, R.K., Sinner, D., Korfhagen, T.R., Reddy, G.B., White, E.S., Jegga, A.G., and Madala, S.K. (2018). Wilms’ tumor 1 drives fibroproliferation and myofibroblast transformation in severe fibrotic lung disease. *JCI Insight* **3**, e121252.
- Sörensen, I., Adams, R.H., and Gossler, A. (2009). DLL1-mediated Notch activation regulates endothelial identity in mouse fetal arteries. *Blood* **113**, 5680–5688.
- Srinivas, S., Watanabe, T., Lin, C.S., William, C.M., Tanabe, Y., Jessell, T.M., and Costantini, F. (2001). Cre reporter strains produced by targeted insertion of EYFP and ECFP into the ROSA26 locus. *BMC Dev. Biol.* **1**, 4.
- Suzuki, T. (1972). Application of scanning electron microscopy in the study of the human spleen: three dimensional fine structure of the normal red pulp and its changes as seen in splenomegalias associated with Banti’s syndrome and cirrhosis of the liver. *Nippon Ketsueki Gakkai Zasshi* **35**, 506–522.
- Suzuki, T., Furusato, M., Takasaki, S., Shimizu, S., and Hataba, Y. (1977). Stereoscopic scanning electron microscopy of the red pulp of dog spleen with special reference to the terminal structure of the cordal capillaries. *Cell Tissue Res.* **182**, 441–453.
- Swirski, F.K., Nahrendorf, M., Etzrodt, M., Wildgruber, M., Cortez-Retamozo, V., Panizzi, P., Figueiredo, J.L., Kohler, R.H., Chudnovskiy, A., Waterman, P., et al. (2009). Identification of splenic reservoir monocytes and their deployment to inflammatory sites. *Science* **325**, 612–616.
- T’Jonck, W., Guilliams, M., and Bonnardel, J. (2018). Niche signals and transcription factors involved in tissue-resident macrophage development. *Cell. Immunol.* **330**, 43–53.
- Schaefer, B.C., Schaefer, M.L., Kappler, J.W., Marrack, P., and Kedl, R.M. (2001). Observation of antigen-dependent CD8+ T-cell/ dendritic cell interactions in vivo. *Cell Immunol.* **214**, 110–122.
- Schaum, N.; Tabula Muris Consortium; Overall coordination; Logistical coordination; Organ collection and processing; Library preparation and sequencing; Computational data analysis; Cell type annotation; Writing group; Supplemental text writing group; Principal investigators (2018). Single-cell transcriptomics of 20 mouse organs creates a Tabula Muris. *Nature* **562**, 367–372.
- Tang, W., Lu, Y., Tian, Q.Y., Zhang, Y., Guo, F.J., Liu, G.Y., Syed, N.M., Lai, Y., Lin, E.A., Kong, L., et al. (2011). The growth factor progranulin binds to TNF receptors and is therapeutic against inflammatory arthritis in mice. *Science* **332**, 478–484.
- van den Brink, S.C., Sage, F., Vértessy, Á., Spanjaard, B., Peterson-Maduro, J., Baron, C.S., Robin, C., and van Oudenaarden, A. (2017). Single-cell sequencing reveals dissociation-induced gene expression in tissue subpopulations. *Nat. Methods* **14**, 935–936.
- Varol, C., Mildner, A., and Jung, S. (2015). Macrophages: development and tissue specialization. *Annu. Rev. Immunol.* **33**, 643–675.
- Vento-Tormo, R., Efremova, M., Botting, R.A., Turco, M.Y., Vento-Tormo, M., Meyer, K.B., Park, J.E., Stephenson, E., Polański, K., Goncalves, A., et al. (2018). Single-cell reconstruction of the early maternal-fetal interface in humans. *Nature* **563**, 347–353.

- Wolf, F.A., Angerer, P., and Theis, F.J. (2018). SCANPY: large-scale single-cell gene expression data analysis. *Genome Biol.* *19*, 15.
- Wolock, S.L., Lopez, R., and Klein, A.M. (2019). Scrublet: Computational Identification of Cell Doublets in Single-Cell Transcriptomic Data. *Cell Syst.* *8*, 281–291.e9, e289.
- Yamamoto, M., Kato, T., Hotta, C., Nishiyama, A., Kurotaki, D., Yoshinari, M., Takami, M., Ichino, M., Nakazawa, M., Matsuyama, T., et al. (2011). Shared and distinct functions of the transcription factors IRF4 and IRF8 in myeloid cell development. *PLoS ONE* *6*, e25812.
- Yu, G., Wang, L.G., Han, Y., and He, Q.Y. (2012). clusterProfiler: an R package for comparing biological themes among gene clusters. *OMICS* *16*, 284–287.
- Yu, X., Buttgereit, A., Lelios, I., Utz, S.G., Cansever, D., Becher, B., and Greter, M. (2017). The Cytokine TGF- β Promotes the Development and Homeostasis of Alveolar Macrophages. *Immunity* *47*, 903–912.e4, e904.
- Zanocco-Marani, T., Bateman, A., Romano, G., Valentinis, B., He, Z.H., and Baserga, R. (1999). Biological activities and signaling pathways of the granulosa/epithelin precursor. *Cancer Res.* *59*, 5331–5340.
- Zhou, B., Ma, Q., Rajagopal, S., Wu, S.M., Domian, I., Rivera-Feliciano, J., Jiang, D., von Gise, A., Ikeda, S., Chien, K.R., and Pu, W.T. (2008). Epicardial progenitors contribute to the cardiomyocyte lineage in the developing heart. *Nature* *454*, 109–113.
- Zhou, X., Franklin, R.A., Adler, M., Jacox, J.B., Bailis, W., Shyer, J.A., Flavell, R.A., Mayo, A., Alon, U., and Medzhitov, R. (2018). Circuit Design Features of a Stable Two-Cell System. *Cell* *172*, 744–757.e17, e717.

STAR★METHODS

KEY RESOURCES TABLE

REAGENT or RESOURCE	SOURCE	IDENTIFIER
Antibodies		
Anti-mouse CD3 (17A2)	Biologend	Cat#100222; RRID: AB_2242784
Anti-mouse CD3 (145-2C11)	BD Biosciences	Cat#553060; RRID: AB_394593
Anti-mouse CD11b (M1/70)	Biologend	Cat#101216; RRID: AB_312799
Anti-mouse CD11c (N418)	Biologend	Cat#117349; RRID: AB_2563905
Anti-mouse CD16/32 (2.4G2)	BD Biosciences	Cat#553142; RRID: AB_394657
Anti-mouse CD31 (390)	BD Biosciences	Cat#740690; RRID: AB_2740374
Anti-mouse CD34 (RAM34)	ebioscience	Cat#50-0341-82; RRID: AB_10596826
Anti-mouse CD45 (30-F11)	BD Biosciences	Cat#564225; RRID: AB_2716861
Anti-mouse CD45 (30-F11)	BD Biosciences	Cat#563709; RRID: AB_2687455
Anti-mouse CD64 (X54-5/7.1)	Biologend	Cat#139311; RRID: AB_2563846
Anti-mouse CD115 (AFS98)	Biologend	Cat#135513; RRID: AB_2562667
Anti-mouse CD140b (28E1)	Cell Signaling Technology	Cat#3169S; RRID: AB_2162497
Anti-mouse CD169 (3D6.112)	Biologend	Cat#142408; RRID: AB_2563621
Anti-mouse B220 (RA3-6B2)	BD Biosciences	Cat#103227; RRID: AB_492876
Anti-mouse B220 (RA3-6B2)	ebioscience	Cat#13-0452-85; RRID: AB_466450
Anti-mouse CCL2 (Polyclonal Goat IgG)	R&D Systems	Cat#AF-479-NA; RRID: AB_354500
Anti-mouse CCL7 (Polyclonal Goat IgG)	R&D Systems	Cat#AF-456-NA; RRID: AB_2071565
Anti-mouse c-kit (2B8)	Biologend	Cat#108114; RRID: AB_493596
Anti-mouse CSF-1 (Polyclonal Goat IgG)	R&D Systems	Cat#AF416; RRID: AB_355351
Anti-mouse Desmin (Polyclonal Rabbit IgG)	Monosan	Cat#PS031; RRID: AB_420229
Anti-mouse ERTR7 (ER-TR7)	Acris Antibodies	Cat#MCA2402
Anti-mouse F4/80 (BM8)	Biologend	Cat#123106; RRID: AB_893501
Anti-mouse F4/80 (BM8)	ebioscience	Cat#13-4801-85; RRID: AB_466658
Anti-GFP (Polyclonal Chicken IgY)	Aves	Cat#GFP-1010; RRID: AB_2307313
Anti-mouse gp38 (8.1.1)	Biologend	Cat#127410; RRID: AB_10613649
Anti-mouse LY6C (HK1.4)	Biologend	Cat#128026; RRID: AB_10640120
Anti-mouse LY6G (1A8)	Biologend	Cat#127604; RRID: AB_1186108
Anti-mouse MARCO (ED31)	Euromedex	Cat#GTX43404; RRID: AB_11162718
Anti-mouse MERTK (Polyclonal Goat IgG)	R&D Systems	Cat#BAF591; RRID: AB_2098563
Anti-mouse MHCII (M5/114.15.2)	Biologend	Cat#107628; RRID: AB_2069377
Anti-mouse NPNT (Polyclonal Goat IgG)	R&D Systems	Cat#AF4298-SP
Anti-mouse NT5E (TY/11.8)	Biologend	Cat#127204; RRID: AB_1089062
Anti-RFP (Polyclonal Rabbit IgG)	Antibodies online	Cat#ABIN1043867
Anti-mouse Sca-1 (D7)	Biologend	Cat#108126; RRID: AB_10645327
Anti-mouse Trem14 (16E5)	Biologend	Cat#143304; RRID: AB_11125372
Anti-mouse VCAM1 (429 (MVCAM.A))	BD Biosciences	Cat#561612; RRID: AB_10896662
Anti-mouse WT1 (CAN-R9(IHC)-56-2))	Abcam	Cat#ab89901
Anti-Chicken CF488A	Biotium	Cat#20166-1; RRID: AB_10854387
Anti-goat CF640R	Biotium	Cat#20179; RRID: AB_10853145
Anti-Rabbit CF568	Biotium	Cat#20098; RRID: AB_10557118
Anti-Rabbit AF647	Jackson immunoresearch	Cat#711-606-152; RRID: AB_2340625
Anti-Rat AF647	Jackson immunoresearch	Cat#712-606-153; RRID: AB_2340696
Anti-Sheep AF647	Jackson immunoresearch	Cat#713-606-147; RRID: AB_2340752

(Continued on next page)

Continued

REAGENT or RESOURCE	SOURCE	IDENTIFIER
Streptavidin, Bv421 conjugated	BD Biosciences	Cat#405226
Biological Samples		
Normal Rat serum	Jackson ImmunoResearch	cat#012-200-120
Normal Mouse serum	ThermoFisher Scientific	cat#31881; RRID: AB_2532173
Chemicals, Peptides, and Recombinant Proteins		
Antigen Fix	Microm Microtech	cat#F/P0016
Anti-biotin microbeads	Miltenyi Biotec	cat# 130-090-485; RRID: AB_244365
Anti-mouse CD11b microbeads	Miltenyi Biotec	cat#130-049-601
Anti-mouse CD45 microbeads	Miltenyi Biotec	cat#130-052-301
Collagenase I	GIBCO	cat#17100017
Collagenase D	Roche, Sigma-Aldrich	cat#11088866001
Corn Oil	Sigma	cat#C8267
CountBright™ Absolute Counting Beads	Life Technologies	cat#C36950
Diphtheria toxin	Merck	cat#322326
Dispase II	Roche, Sigma-Aldrich	cat#04942078001
DNase I	Roche, Sigma-Aldrich	cat#11284932001
Dnase I	Sigma	cat#10104159001
FcR blocking reagent, human	Miltenyi Biotec	Cat#130-059-901
Glutaraldehyde 25%	Sigma-Aldrich	Cat#G5882
HEPES	GIBCO	Cat#12509079
Liberase TM Research Grade	Roche, Sigma-Aldrich	Cat#5401119001
2-mercaptoethanol	Sigma	Cat#3148
Paraformaldehyde	Sigma-Aldrich	Cat#0571709
RapiClear 1.47	SunJin Lab	RC147002
Tamoxifen	Sigma	cat#T5648
tamox chow	Envigo	TD.130856
Tissue Freezing Medium	Triangle Biomedical Sciences	72593; cat#100496-345
TB Green Premix Ex Taq	Takara	cat#RR820B
Critical Commercial Assays		
Mouse M-CSF quantikine ELISA kit	R&D systems	Cat#MMC00
Prussian Blue Test Kit	Sigma	Cat#HT20-1KT
RNEasy Plus Micro Kit	QIAGEN	Cat#74034
Quantitect Reverse Transcription Kit	QIAGEN	Cat#205311
Deposited Data		
Murine RNA-sequencing data	This paper	GEO: GSE 148356
Experimental Models: Organisms/Strains		
Mouse: C57BL/6	Janvier Labs	N/A
Mouse: C57BL/6J CD45.1	Charles River Laboratories	N°2014
Mouse <i>Ccl19^{Cre}: C57BL/6N-Tg(Ccl19-cre)489Biat/Biat</i>	EMMA mouse repository	EM:09381
Mouse <i>Ccl2-RFP^f: B6.Cg-Ccl2tm1.1Pame/J</i>	The Jackson Laboratory	JAX: 016849
Mouse <i>Ccr2^{-/-}: B6.129S4-Ccr2tm1fc/J</i>	The Jackson Laboratory	JAX: 004999
Mouse: <i>CD64^{DTR}</i>	Baranska et al., 2018	Gift from Bernard Malissen (CIML, France)
Mouse: <i>Cdh5^{CreERT2}</i>	Sörensen et al., 2009	Gift from Ralf Adams (Muenster, Germany)
Mouse: <i>Csf1^{flox/flox}</i>	Harris et al., 2012	Gift from Sherry Abboud Werner (San Antonio, US)
Mouse <i>Cx3cr1^{GFP}: B6.129P2(Cg)-Cx3cr1^{tm1Litt}/J</i>	The Jackson Laboratory	JAX: 5582
Mouse <i>Rosa^{DTR}: C57BL/6-Gt(ROSA)26Sor^{tm1(HBEGF)Awai}/J</i>	The Jackson Laboratory	JAX: 007900
Mouse: <i>Rosa^{RFP}</i>	Luche et al., 2007	N/A

(Continued on next page)

Continued

REAGENT or RESOURCE	SOURCE	IDENTIFIER
Mouse Rosa ^{tdT} : B6.Cg-Gt(ROSA)26Sortm14(CAG-tdTomato)Hze/J	Madisen et al., 2010;The Jackson Laboratory	JAX: 007914
Mouse Rosa ^{YFP} : B6.129X1-Gt(ROSA)26Sor ^{tm1(EYFP)Cos} /J	The Jackson Laboratory	JAX:006148
Mouse Ubc ^{GFP} : C57BL/6-Tg(UBC-GFP)30Scha/J	The Jackson Laboratory	JAX: 004353
Mouse: Ubow/ Ubc ^{tdTOM}	Ghigo et al., 2013	N/A
Mouse Wt1 ^{CreERT2} : Wt1tm2(cre/ERT2)Wtp/J	The Jackson Laboratory	JAX: 010912
Mouse Wt1 ^{GFP-Cre} : Wt1tm1(EGFP/cre)Wtp/J	The Jackson Laboratory	JAX: 010911
Oligonucleotides		
cell-surface associated Csf1 qPCR FWD CCACTTGTAGAACAGGAGGCC	Rubin et al., 1996	N/A
cell-surface associated Csf1 qPCR REV CCAAGAAGTGAACAACAGCTTTGC	Rubin et al., 1996	N/A
soluble Csf1 qPCR FWD CCACTTGTAGAACAGGAGGCC	Rubin et al., 1996	N/A
soluble Csf1 qPCR REV GCTTGAGGGCAAGAGAAGTACC-3	Rubin et al., 1996	N/A
Software and Algorithms		
BD FACS Diva Software	BD Biosciences	http://www.bdbiosciences.com/us/instruments/clinical/software/flow-cytometry-acquisition/bd-facsdiva-software/m/333333/overview
CellPhoneDB	Teichmann Lab and Vento-Tormo Lab (Wellcome Sanger Institute, Cambridge, UK)	www.cellphonedb.org ; RRID: SCR_017054
Illustrator, CC2015	Adobe	https://www.adobe.com/ ; RRID: SCR_010279
ImageJ	Schneider et al., 2012	https://imagej.nih.gov/ij/ ; RRID: SCR_018407
Imaris, v8	Bitplane	http://www.bitplane.com ; RRID: SCR_007370
Photoshop, CC2015	Adobe	http://www.adobe.com/ ; RRID: SCR_014199
Prism, v7	GraphPad Software	https://www.graphpad.com/scientific-software/prism/ ; RRID: SCR_002798
Zeiss ZEN 2010	Carl Zeiss	http://www.zeiss.com

RESOURCE AVAILABILITY

Lead Contact

Further information and requests for resources and reagents should be directed to Marc Bajénoff (bajenoff@ciml.univ-mrs.fr).

Materials Availability

Materials generated in this study will be available from the authors upon request to bajenoff@ciml.univ-mrs.fr.

Data and code availability

All RNA-sequencing data have been deposited in the Gene Expression Omnibus public database as Database: GSE148356.

EXPERIMENTAL MODEL AND SUBJECTS DETAILS

Mice

Mice were maintained under specific pathogen free conditions and a 12 h light/dark cycle at an ambient temperature of 22°C at the animal facilities of the CIML (Marseille, France). Animals were housed in individually ventilated cages containing sterile quarter-inch corncob bedding and cotton pads for environmental enrichment. All experiments were performed in accordance with the French ethical committee. Unless otherwise specified, a mix of male and female mice were used for each experiment and mice were considered adult at the age of 6 weeks. C57BL/6 mice were purchased from Janvier Labs. CD45.1 (Ly5.1) mice were purchased from Charles River. Ubc^{tdT} mice were generated as previously described (Ghigo et al., 2013; Luche et al., 2007). Rosa^{tdT} (also known as Ai14, (Madisen et al., 2010)), Rosa^{DTR} (Buch et al., 2005), Rosa^{YFP} (Srinivas et al., 2001), Cx3cr1^{GFP} (Jung et al., 2000), Ccr2^{-/-} (Boring et al., 1997), Wt1^{CreERT2} (Zhou et al., 2008), Wt1^{GFP-Cre} (Zhou et al., 2008), Ccl2-RFP^{fl} (Shi and Pamer, 2011), Ubc^{GFP} (Schaefer

et al., 2001) mice were purchased from the Jackson Laboratory. *Ccl19^{Cre}* mice (Chai et al., 2013) were purchased from the EMMA mouse repository (Vienna, Austria). *Csf1^{flox/flox}* (Harris et al., 2012), *Cdh5-CreERT2* (Sørensen et al., 2009) and *CD64^{DTR}* mice (Baranska et al., 2018) were a kind gift from respectively Sherry Abboud Werner (San Antonio, US), Ralf Adams (Muenster, Germany) and Bernard Malissen (CIML, France).

METHOD DETAILS

Tamoxifen administration

Adult mice were gavaged once per week with 15mg of regular tamoxifen dissolved in corn oil (both from Sigma-Aldrich), twice (*Wt1^{CreERT2} Rosa^{tdT}*, *Wt1^{CreERT2} Rosa^{tdT} CD64^{DTR}*) or three times (*Wt1^{CreERT2} Rosa^{YFP/DTR}*). Adult *Cdh5^{CreERT2} Csf1^{flox/flox}* mice were fed with tamox chow (Envigo) for one month.

Bone marrow chimeras

For shield irradiation, anesthetized mice were placed into a 6mm thick lead cylinder to selectively expose their hind legs to irradiation, but protect (shield) the rest of their body. To generate regular BM chimeras, mice were subjected to full-body irradiation. Mice were irradiated (9Gy) and reconstituted with at least $\sim 3 \times 10^6$ total bone marrow (BM) cells prepared using standard procedures.

Isolation of RPM, splenic stromal cells, and lymph node FRC

For splenic stromal cell isolation, spleens were injected *in situ* with warm RPMI medium (Invitrogen) containing 400U/mL Collagenase I (GIBCO) with 30 G syringe and harvested 2min later. Cell suspensions from adult mouse spleens and lymph nodes were obtained through mechanical dissociation and enzymatic digest. Briefly, organs were harvested, finely minced with scissors and digested in RPMI medium containing 3mg/mL Collagenase D (Roche), 0,8 mg/mL Dispase II (Roche), 0,1 mg/mL DNase I (Roche), 2% FCS, 5% Supplementum Complementum (Penicillin/Streptomycin 1000U/mL, 40mM L-glutamin, 100mM HEPES (GIBCO), 1mM β -mercaptoethanol (Sigma) in RPMI medium). Digests were performed for 40min at 37°C under continuous agitation (1000rpm) with resuspension and collection of supernatant every 20min to FACS buffer (PBS, 1%FCS, 2mM EDTA). Samples were regularly pipetted up and down to support mechanical dissociation and digest. Cell suspensions obtained from the spleen were subjected to red blood cell lysis prior to enrichment/staining. To enrich splenic and lymph node fibroblastic stromal cells, hematopoietic cells were depleted by incubating the cell suspension with MACS anti-CD45 microbeads (Miltenyi Biotec) and passing them through a MACS LS column (Miltenyi Biotec). Unbound single-cell suspensions were used for further flow cytometric analysis.

Flow cytometry

Blood samples were drawn from the retro-orbital vein and subjected to RBC lysis prior to staining. Bone Marrow cell suspensions were obtained from mice tibia by flushing the bones with PBS, filtering the suspensions on a 70 μ m cell strainer and lysing red blood cells. Peritoneal and pleural washouts were performed by intraperitoneal and intrathoracic injections of cold PBS (5 and 2ml respectively) and collection of the resulting fluids. Single cell suspensions were stained blocked in a medium containing rat serum, mouse serum and CD16/32 specific blocking antibody (Biolegend). Surface staining was then performed in FACS buffer for 30min at 4°C. Data were acquired on a LSRII 561 (Becton Dickinson) and analyzed using Diva software (BD) and Prism7 (GraphPad). RP Fibroblasts and FRC were sorted using a FACS Aria IIIu (BD, Biosciences).

Immunostaining for confocal microscopy

Spleens and lymph nodes were fixed in AntigenFix (Microm Microtech) for 2 h at RT and washed in 0.1M phosphate buffer. For vibratome sections, one hundred and fifty μ m-thick sections were prepared and stained with the indicated antibodies in IHC buffer (Tris 0.1M, BSA 0.5%) containing 2% Triton X-100 for a minimum of 4 h. After 30min washing, spleen sections were clarified with Rapiclear 1.47 (SunJin Lab) for 2 h. For cryostat sections, organs were dehydrated in 30% sucrose in 0.1M phosphate buffer for 12 h, embedded in tissue freeze medium (Triangle Biomedical Sciences) and snap frozen. Twenty μ m-thick sections were prepared and stained with the indicated antibodies in IHC buffer containing 2% Triton X-100 for minimum 2 h. Confocal images were acquired on a Zeiss LSM 880 confocal microscope. Final image processing was done using Imaris software (Bitplane) and Adobe Photoshop.

Iron Staining

For Perl's Prussian Blue stain, spleens were fixed with 4% formaldehyde in 0.1M phosphate buffer (pH 7.0) for 3 h, embedded in paraffin, and stained with Perl's Prussian blue and Pararosaniline (Sigma).

Scanning Electron Microscopy

Spleens were fixed in Antigen Fix for 2 h and cut with a vibratome into 250 μ m thick slices. Spleen slices were post-fixed in 2% PFA, 2.5% glutaraldehyde in PBS overnight at 4°C. The next day, the samples were washed three times in PBS and dehydrated in graded series of ethanol baths (10min each). The samples were freeze-cracked with a razor blade in parafilm packs submerged in liquid nitrogen. Once air-dried, the samples were placed on carbon taped-stubs with the cracked face up for gold sputtering (10' at 15mA, Edwards). Imaging was carried out on an FEI Teneo VS running in high vacuum, at 10kV and using an ETD secondary electrons detector.

Antibodies

Specific antibodies directed against mouse CD11b (M1/70), CD64 (X54-5/7.1), F4/80 (BM8), MHCII (M5/114.15.2), CD3 (17A2), LY6C (HK1.4), LY6G (1A8), CD115 (AFS98), gp38 (8.1.1), NT5E (TY/11.8), Trem14 (16E5), Sca-1 (D7), c-kit (2B8), CD169 (3D6.112) were purchased from Biolegend. B220 (RA3-6B2), CD3 (145-2C11), CD45 (30-F11), VCAM1 (429 (MVCAM.A)), CD31 (390), CD16/32 (2.4G2) antibodies were purchased from BD. ERTR7 (ER-TR7), CD140b (28E1), WT1 (CAN-R9(IHC)-56-2)), CD34 (RAM34), MARCO (ED31) specific antibodies were purchased respectively from Acris antibody, Cell Signaling, Abcam, ebioscience and Euromedex. CSF-1, CCL2, CCL7, NPNT, MerTK (Polyclonal Goat IgG) specific antibodies were purchased from R&D systems. GFP (Polyclonal Chicken IgY), RPF (Polyclonal Rabbit IgG), Desmin (Polyclonal Rabbit IgG) specific antibodies were purchased respectively from Aves, Antibodies online and Monosan. Chicken CF488, Rabbit CF568 and goat CF640R specific antibodies were purchased from Biotium. Rabbit AF647, Rat AF647 and Sheep AF647 specific antibodies were purchased from Jackson immunoresearch.

Diphtheria toxin mediated RPM or RP Fibroblasts depletion

Diphtheria toxin (DTx) (Merck) was dissolved in PBS and stored at -80°C . Isoflurane anaesthetized *Cx3cr1^{GFP}*, *CD64^{DTR}*, *CD64^{DTR} Cx3cr1^{GFP}*, *Wt1^{CreERT2} Rosa^{tdT} CD64^{DTR}* or *Wt1^{CreERT2} Rosa^{YFP/DTR}* mice were injected in the retro-orbital venous sinus with a single dose of 1 μg of DTx or PBS for control mice. Mice were sacrificed at the indicated time points and spleens were harvested for analysis.

Monocyte transfer

DTx-treated *CD64^{DTR}* mice were injected in the retro-orbital venous sinus with monocytes collected from the spleen and BM of adult *Ubc^{tdT}* mice (regular transfer) or adult *Ccr2^{WT} Cx3cr1^{GFP/+} Ubc^{tdT}* and *Ccr2^{KO} Cx3cr1^{GFP/+}* mice (competitive transfer). For spleen monocytes, the spleens were harvested and digested as previously described. For BM monocytes, tibias and femurs were flushed with cold PBS and the suspension was filtered on a 70 μm cell strainer. Monocyte enrichment was achieved by negative selection of neutrophils, T and B cells using biotin-conjugated anti-CD3-, CD45B-, Ly-6G Abs followed by anti-biotin microbeads (Miltenyi Biotec). Cell suspensions were then similarly enriched for *CD11b⁺* cells. Enriched cells were labeled with fluorescent antibodies and *CD11b⁺ CD117⁻* monocytes were sorted using a FACS Aria IIIu.

Spleen grafting

Inguinal lymph nodes were surgically removed from *Ubc^{GFP}* mice under general anesthesia. One ~ 3 mm-thick fragment of spleen collected from WT (Figure S5E) or *Wt1^{ΔCcl2}* and littermate controls (Figure 5F) was transplanted into the lymph node-free inguinal pockets of *Ubc^{GFP}* mice (*Wt1^{ΔCcl2}* in the right pocket, control in the left pocket). Animals were maintained under Ibuprofen in drinking water (0,1mg/mL) for the entire duration of the experiment.

Bulk RNA Sequencing and bioinformatics analysis

Wt1^{CreERT2} Rosa^{tdT} CD64^{DTR} mice received tamoxifen as previously described and were treated (“RPM depletion”, Figure 5) or not (“steady state”, Figures 2, S1) one week later with DTx. 12 h later, RP Fibroblasts (“steady state” and “RPM depletion”) and FRC (“steady state”) were FACS-purified into 350 μL RLT Buffer (QIAGEN) from the spleens and lymph nodes respectively. Biological triplicates were generated from a pool of 2 mice per sample. Total RNA was extracted using RNeasy Plus micro kit (QIAGEN) following the manufacturer’s instructions. Library preparation and RNA sequencing were performed by the IGBMC GenomEast platform, a member of the ‘France Génomique’ consortium (ANR-10-INBS-0009). Sequencing was performed using an Illumina HiSeq 4000 sequencer. On the platform, reads were preprocessed in order to remove adaptor and low-quality sequences (Phred quality score below 20). After this preprocessing, reads shorter than 40 bases were discarded for further analysis. These preprocessing steps were performed using cutadapt version 1.10. Reads were mapped to rRNA sequences using bowtie version 2.2.8, and reads mapping to rRNA sequences were removed for further analysis. Successively, remaining reads were mapped onto the mm10 assembly of *Mus musculus* genome using STAR version 2.5.3a. Gene expression quantification was performed from uniquely aligned reads using htseq-count version 0.6.1p1, with annotations from Ensembl version 93 and “union” mode. Successive analysis were performed using homemade R scripts with R version 3.5.3. Analysis of differential expression of genes (DEG) was done thanks to the DESeq2 R packages (version 1.20.0) using a negative binomial generalized linear model. Data normalization was done using the FRC and RP fibroblast replicates all together in the DESeq2 model with shrunken log2 fold changes (LFC) and SE. Volcano plot of differentially expressed genes between FRC and RP fibroblasts uses statistics generated by the DEG analysis (LFC and adjusted p value). Highlighted genes come from (Malhotra et al., 2012). Heatmaps comparing FRC and RP fibroblast populations were created using pheatmap R package (version 1.0.12). In Figure 2F, the displayed genes are the top 30 genes computed by the DEG analysis considering both the genes LFC and their DEG adjusted p value (adj-pval < 0.05). Heatmap displaying chosen list of genes were created using pheatmap R package (version 1.0.12). Enrichment analysis of Gene Ontology terms (Biological Processes) was done using genes selected (i) from the DEG analysis (adj-pval < 0.05) and (ii) having a mean expression greater than 1000 in at least FRC and RP fibroblasts and a LFC greater than 2 between the two populations. This selection identified 358 genes overexpressed in RP fibroblasts versus FRC. The R package ClusterProfiler (version 3.8.1) was used to perform the enrichment analysis based on these genes. Biological processes were selected among the top enriched ones on their interest in the study and grouped by biological function.

Murine spleen scRNaseq data analysis

Fastq files from E-MTAB-7703 (Cheng et al., 2019) and the Tabula Muris (10X droplet sequencing) spleen samples (P4_7, P7_6) (Schaum et al., 2018) were downloaded. These data were processed to count matrices using the kallisto and bustools workflow, pseudoaligning reads to the GRCm38 reference (Melsted et al., 2019). Data were subsetted to cells with total features > 500, and percent mitochondrial counts < 10%. Downstream analysis was conducted using Scanpy (Wolf et al., 2018). Data were normalized and log transformed before calling the top 2000 highly variable genes, and calculating the first 30 principal components. Principal component coordinates were used in neighbor graph construction and UMAP embedding. We calculated clusters on the graph using the Leiden algorithm, with resolution = 1. Clusters were annotated to cell types using canonical immune cell markers, and genes described in (Cheng et al., 2019). The splenic stroma dataset was subset to cells annotated as red pulp fibroblasts and we conducted a repeated clustering analysis using the Leiden algorithm with resolution parameter set to 0.4. Dissociation stress gene sets were downloaded from (Bhattacharya et al., 2018; van den Brink et al., 2017). Ligand-receptor interaction analysis was performed using the python implementation of CellPhoneDB version 2.0, setting threshold = 0.2 (Egen et al., 2008; Vento-Tormo et al., 2018). Analysis of chemokine and cytokine genes was performed using a gene list downloaded from immport (Bhattacharya et al., 2018). Enrichment of gene lists for Gene Ontology, REACTOME, and KEGG terms was conducted with the ClusterProfiler R package (Yu et al., 2012). Identification of active transcription factor regulons was conducted using the PyScenic toolkit (Aibar et al., 2017).

Human spleen processing

Human spleen samples (n = 2) were collected from recently deceased donors and cut into approx 30 mm³ pieces before digestion in a solution containing 25 µg/mL Liberase TM (Roche) and 50 µg/mL DNase (Sigma) in 5 mL RPMI (GIBCO) for 30min at 37°C. The sample was then dissociated using mechanical disruption over a 70 µm sieve, and resulting suspension washed with PBS. Subsequently samples were processed as follows: Experiment 1: Splenocytes were FACS sorted into CD45⁺ and CD45⁻ fractions. Experiment 2: Cells were incubated with saturating concentrations of FcR blocking reagent (Miltenyi Biotec) for 10min at room temperature, then stained with a lineage mixture of FITC-conjugated anti-CD3 (Hit3a) (Tonbo biosciences), FITC-conjugated anti-CD19 (SJ25C1) (Biolegend), FITC-conjugated anti-CD56 (5.1H11) (Biolegend), FITC-conjugated anti-CD138 (DL101) (eBioscience), and FITC-conjugated anti-TCRαβ (IP26) (Invitrogen) for 15min at room temperature. We performed negative selection with anti-FITC microbeads (Stem Cell Technologies) according to manufacturer's instructions.

Separately, cells were stained with FITC-conjugated anti-CD45 (2D1) (Biolegend). We again performed negative selection with anti-FITC microbeads (Stem Cell Technologies) according to manufacturer's instructions.

The lineage negative and CD45⁻ suspensions were counted using an haemocytometer and adjusted to 1000 cells/µL. Cells were loaded onto the Chromium 10X microfluidics controller and processed using the standard protocol. Experiment 1 used 10X version 2 chemistry; experiment 2 used 10X version 3 chemistry.

Sequencing was performed on an Illumina HiSeq 4000 instrument.

Human spleen scRNaseq analysis

Count matrices were calculated using the cellranger software package version 3 (10X genomics). Features were subsetted to the intersect of features mapped between the two chemistries. Data were subsetted to cells with total features > 250, and percent mitochondrial counts < 20%. We removed computationally predicted doublets using the Scrublet tool (Wolock et al., 2019), using default settings. Data were normalized and log transformed before calling the top 2000 highly variable genes using Scanpy. Data were integrated between each experiment using the fastMNN function in the Batchelor R package (Haghverdi et al., 2018), before using these corrected principal component coordinates to calculate a neighbor graph, UMAP embedding, and Leiden clustering solution in Scanpy. Clusters were annotated to cell types using canonical immune cell markers. We mapped murine genesets to orthologs using bioMart (Smedley et al., 2009) in R, and calculated enrichment scores using Scanpy.

Dosage of serum CSF1

After collection, the blood was allowed to clot by leaving it undisturbed at room temperature for 30min. The clot was removed by centrifuging at 10 000 rpm for 5min at 4°C. The collected supernatant was further centrifuged under the same conditions and the collected sera were stored at -20°C. The levels of circulating CSF1 were determined using the mouse M-CSF quantikine ELISA kit (R&D systems) following the manufacturer's instructions. Optical density was determined using the microplate reader Spectrostar Omega (BMG labtech).

qRT-PCR

Splenic stromal cells and CD45⁺ cells from adult wild type, *Ccl19*^{-Δ*Csf1*} and *Wt1*^{-Δ*Csf1*} mice (pool of 3 mice per sample) were FACS-sorted and total RNA was extracted as previously described. Quantitative reverse transcriptase-polymerase chain reaction (RT-PCR) was performed (Quantitect Reverse Transcription Kit, QIAGEN) with SYBR Green PCR master mix (TB Green Premix Ex Taq, Takara). The reaction was carried out in an 7500 Fast Real Time PCR system (Applied Biosystems), one cycle 95°C 20 s followed by 40 cycles 95°C 3 s 60°C 30 s. Primers used included soluble CSF-1 (Pa:5'-CCACTTGTAGAACAGGAGGCC-3'; Pb: 5' GCTTGAGGGCAAGAGAAGTACC-3'), cell-surface associated CSF-1 (Pa:5'-CCACTTGTAGAACAGGAGGCC-3'; Pc: 5'

CCAAGAACTGCAACAACAGCTTTGC-3') (Rubin et al., 1996), and glyceraldehyde-3-phosphate dehydrogenase (*Gapdh*) (5'-GGGTGTGAACCACGAGAAAT-3', 5'-CCTTCCACAATGCCAAAGTT-3'). The average CT value for each gene was calculated and normalized to *Gapdh*.

QUANTIFICATION AND STATISTICAL ANALYSIS

Quantification of YFP⁺ pixels in the Red Pulp

Same size/thickness confocal images of spleen sections were made in DTX treated and untreated *Wt1^{CreERT2} Rosa^{YFP/DTR}* mice. RP was identified through F4/80 staining. In this region, the area covered by YFP⁺ pixels was determined using ImageJ software (see also legend of [Figure S3A](#)).

Quantification of cells

In order to quantify the absolute numbers of cells present in a given blood volume or weighed spleen piece or graft, CountBright Absolute Counting Beads (Life Technologies) were added to the samples before flow cytometry analysis. These numbers were determined using the bead-to-cell ratio.

Statistical analysis

Mean values were calculated using Prism software (GraphPad) as indicated in the respective figures. p values were calculated with the Mann-Whitney test. ns: $p > 0.05$, * $p < 0.05$, ** $p < 10^{-2}$, *** $p < 10^{-3}$, **** $p < 10^{-4}$